QATAR UNIVERSITY

COLLEGE OF ARTS AND SCIENCES

ER DOPED III-NITRIDE SEMICONDUCTORS

BY

YAHYA ZAKARIA

A Thesis Submitted to the Faculty of

the College of Arts and Sciences

in Partial Fulfillment

of the Requirements

for the Degree of

Masters of Science

in

Material Science and Technology

June 2017

© 2017 Yahya Zakaria. All Rights Reserved.

COMMITTEE PAGE

The members of the Committee approve the Thesis of Yahya Zakaria defended on 25/05/2017.

____

Dr. Talal Al Tahtamouni
Thesis/Dissertation Supervisor

____

Dr. Ahmed Elzatahry
Committee Member

____

Dr. Nasr Bensalah
Committee Member

____

Dr. Xiaohang Li
Committee Member

____

Approved:

____

Rashid Al-Kuwari, Dean, College of College of Arts and Sciences

ABSTRACT

ZAKARIA YAHYA, Masters : June : [2017], Material Science and Technology

Title: Er Doped III-Nitride Semiconductors

Supervisor of Thesis: Talal Al tahtamouni.

Erbium ions (Er^{3+}) doped in a solid material enables the intra 4f shell transitions from its first excited state ($4I_{13/2}$) to the ground state ($4I_{15/2}$). The intra-4f shell transition at 1540 nm is of exceptional interest as the wavelength matches the minimum loss region of silica fibers used in optical communications. Aluminium nitride (AlN) as host material for Erbium (Er) has attracted a lot of interest due to its physical and chemical properties such as the wide bandgap. Metal-Organic Chemical Vapor Deposition (MOCVD) is the most advanced state-of-art growth technique which provides both high quality single crystal thin film deposition capability and high growth rate. MOCVD is a versatile technique that widely used in research laboratories and in industrial factories.

In this thesis, the effects of Er flux on MOCVD grown Er:AlN properties were investigated using different characterization techniques such as X-ray Diffraction (XRD), Photoluminescence (PL) Spectroscopy, Secondary Ion Mass Spectroscopy (SIMS), X-ray Photoelectron Spectroscopy (XPS), Scanning Electron Microscopy (SEM) and Atomic Force Microscopy (AFM).

XRD θ-2θ scans showed strong peak (002) for AlN and sapphire substrate (Al_2O_3), and the absence of any secondary phase for all samples. Rocking curve scans

showed that increasing the Er flux increases the full width at half maximum (FWHM) of the symmetric (002) planes for AlN:Er. Surface imaging studies showed that increasing Er flux increases the surface roughness. SIMS profiles revealed that Er is uniformly distributed throughout the doped layers and enabled the direct measurement of the doped layer thickness using optical profiler. XPS exhibited the surface quantitative measurement of Aluminium, Nitrogen, Oxygen, and Carbon. PL measurements revealed that increasing the Er flux increases the 1.54µm emission intensity.

DEDICATION

To my mother, the greatest mother in the world, whom I owe everything in my life. To my father, fiancé and sisters.

ACKNOWLEDGMENTS

All praise is due to Allah for his blessings and guidance. I would like to express my sincere gratitude and acknowledgment to my family especially my mother Houda Halima.

I would like to express my acknowledgments and gratitude to my professor and supervisor, Dr. Talal Altahtamouni for his constant support, motivation, professionalism and guidance during my thesis research. I also would like to express my acknowledgement and gratitude to the committee members of this thesis Dr. Ahmed Elzatahry, Dr. Nasr Bensalah, Dr. Ahmed Ennaoui from HBKU and Dr. Xiaohang Li from KAUST. I would like to thank the professors at material science and technology program who provided me with the right knowledge and skill-set for material science research, Prof. Mariam Al Maadeed, Dr. Khaled Yousuf, Dr. Abubakr Abdullah. I would like to acknowledge also the support of the master program coordinator Mrs. Sharon Saldanha.

Special thanks to all family members, colleagues and friends who supported this work namely Katie Melling, Nicolas Barth, Fanilo Ramasomanana.

TABLE OF CONTENTS

ACKNOWLEDGMENTS vi
LIST OF TABLES ix
LIST OF FIGURES x
CHAPTER 1: INTRODUCTION 1
CHAPTER 2: LITERATURE REVIEW 4
1. III-Nitride Materials 4
2. III-Nitrides chronological development 7
3. Aluminium Nitride (AlN) crystalline properties 8
4. Thermodynamic and chemical properties of AlN 11
5. Mechanical properties of AlN 12
6. Band structure and electrical properties of AlN 12
7. Rare earth doped semiconductors 13
8. Erbium doped semiconductors 15
9. Erbium doped AlN 19
CHAPTER 3: EXPERIMENTAL TECHNIQUES 22
1. Metalorganic Chemical Vapor Deposition (MOCVD) 22
2. X-ray Diffraction 25
3. Photoluminescence (PL) spectroscopy 29
4. Surface Analysis 33
a. X-ray Photoelectron Spectroscopy 35
b. Time of Flight – Secondary Ion Mass Spectroscopy (TOF-SIMS) 41
5. Surface Imaging 45
a. Scanning Electron Microscopy (SEM) 45
b. Atomic Force Microscopy (AFM) 48
CHAPTER 4: RESULTS AND DISCUSSION 51
1. MOCVD Growth of Er doped AlN 51
2. Structural properties 54
3. Surface analysis (chemical composition) 63
a. X-ray Photoelectron Spectroscopy 63
b. Time of Flight - Secondary Ion Mass Spectrometer 69
4. Surface morphology 75

a. Scanning Electron Microscopy. 75
b. Atomic Force Microscopy 78
5. Optical properties.......... 81
CHAPTER 5: CONCLUSION 85
FUTURE WORK.......... 87
REFERENCES 88

LIST OF TABLES

Table 2-1. Standardized crystallographic data. 10

Table 4-1. Erbium flux and growth temperature for AlN:Er samples. 53

Table 4-2. FWHM of AlN:Er samples. 61

Table 4-3. Metallic Al, Al-N state Al and Al-O state Al binding energies. 64

Table 4-4. Surface atomic concentration for Er:AlN (32) using narrow scans. 68

Table 4-5. Surface atomic concentration for un-doped AlN using narrow scans including Al chemical states. 69

Table 4-6. Surface roughness measurements for AlN:Er samples. 78

LIST OF FIGURES

Figure 2-1. Chemical elements in III-V compound semiconductors. 5
Figure 2-2. Band-gap and lattice parameter for III-Nitride materials. 5
Figure 2-3. n-type and p-type AlN. 6
Figure 2-4: Photon emission process – direct and indirect band gap. 7
Figure 2-5. Aluminum Nitride Wurtzite structure. 9
Figure 2-6. Aluminium Nitride structure represented as tetrahedral units of [AlN4]. 9
Figure 2-7. Powder X-ray Diffraction for AlN. 10
Figure 2-8. Bandgap structure of wurtzite AlN. 13
Figure 2-9. Energy level chart of certain trivalent rare earth elements (Er3+, Eu3+, Tm3+, Pr^{3+}*) in GaN.* 14
Figure 2-10. Optical loss for optical fibers as a function of signal wavelength 16
Figure 2-11. Erbium Doped Fiber Amplifier device. 16
Figure 2-12. Erbium Doped Fiber Amplifier basic principle. 17
Figure 2-13. Energy levels of the trivalent Er^{3+} *4f electrons at 1.54 µm.* 17
Figure 2-14. Er^{3+} *emission in different host materials in different temperatures.* 19
Figure 2-15: Sapphire unit cell. 21
Figure 2-16: c-plane AlN on c-plane Sapphire 21
Figure 3-1. Example of InP MOCVD growth schematic using TMIn and PH3 precursors. 23
Figure 3-2. Schematic diagram for MOCVD main components. 24
Figure 3-3. Image of MOCVD VEECO system. 25
Figure 3-4. X-ray diffraction schematics. 26
Figure 3-5. X-ray diffraction principle. 26
Figure 3-6. X-ray diffraction equipment. 28
Figure 3-7. X-ray tube schematics. 29
Figure 3-8. Energy diagram for photoluminescence process. 30
Figure 3-9. PL System schematics. 31
Figure 3-10. Schematic diagram of the PL spectrometer. 32
Figure 3-11. Longwavepass filter spectrum. 32

Figure 3-12. Top view of the optical path...33

Figure 3-13. Analytical resolution & detection limit for the most common characterization tools. 35

Figure 3-14. Schematic of photoelectric effect. 37

Figure 3-15. Schematic of electrons energy levels in photoelectric process...................37

Figure 3-16. Survey spectrum for un-doped AlN thin film 39

Figure 3-17. Schematics for main XPS components. 40

Figure 3-18. X-ray Monochromator in XPS...41

Figure 3-19. XPS spectra with and without Monochromator...41

Figure 3-20. TOF-SIMS basic principle...43

Figure 3-21. Schematic of TOF – mass analysis. 44

Figure 3-22. TOF-SIMS spectrum for PET sample...45

Figure 3-23. Comparison between the wavelength of a 60 kV electron and visible light.46

Figure 3-24. Basic components of Scanning Electron Microscope. 47

Figure 3-25. Scanning electron microscopy interaction zones and related emissions. 48

Figure 3-26: AFM cantilever and tip schematic...49

Figure 3-27: Probe deflection sensing schematic...50

Figure 4-1. Growth temperature sequence of the Er doped AlN epilayer growth on sapphire substrate. 52

Figure 4-2. Un-doped AlN layers structure...53

Figure 4-3. AlN:Er layers structure. 53

Figure 4-4. XRD theta-2theta scan for un-doped AlN on Sapphire................................56

Figure 4-5. XRD theta-2theta scan for AlN:Er (20) sample c-plane AlN on Sapphire....56

Figure 4-6. XRD theta-2theta scan for AlN:Er (24) sample c-plane AlN on Sapphire....57

Figure 4-7. XRD theta-2theta scan for AlN:Er (28) sample c-plane AlN on Sapphire....57

Figure 4-8. XRD theta-2theta scan for AlN:Er (32) sample c-plane AlN on Sapphire.....58

Figure 4-9. Rocking curve measurements for un-doped AlN..59

Figure 4-10. Rocking curve measurements for the sample Er:AlN (20).........................59

Figure 4-11. Rocking curve measurements for the sample AlN:Er (24).........................60

Figure 4-12. Rocking curve measurements for the sample AlN:Er (28).........................60

Figure 4-13. Rocking curve measurements for the sample AlN:Er (32).........................61

Figure 4-14. Rocking curve measurements overlaid for all AlN:Er samples.................62

Figure 4-15: FWHM of (002) rocking curve of Er:AlN as a function Erbium flux. 62
Figure 4-16. XPS Survey spectrum for un-doped AlN....65
Figure 4-17. XPS Al2p narrow scan for Er:AlN (32)...66
Figure 4-18. XPS N1s narrow scan for Er:AlN (32)....66
Figure 4-19. XPS C1s narrow scan for Er:AlN (32)....67
Figure 4-20. XPS O1s narrow scan for Er:AlN (32)....67
Figure 4-21. Narrow scan Al2p spectrum fitting for Er:AlN (32). 68
Figure 4-22. Er:AlN (32) surface before sputtering. 70
Figure 4-23. Er:AlN (32) surface after sputtering. 71
Figure 4-24. Er^+ TOF-SIMS profiles for Er:AlN (28) and Er:AlN (32) in linear scale as a function of sputtering time. 73
Figure 4-25. Er^+ TOF-SIMS profiles for Er:AlN (28) and Er:AlN (32) in linear scale as a function of depth....73
Figure 4-26. TOF-SIMS profiles for Er:AlN (28) in log scale as a function of depth. 74
Figure 4-27. TOF-SIMS profiles for Er:AlN (32) in log scale as a function of depth. 74
Figure 4-28. SEM image for AlN:Er (20)...76
Figure 4-29. SEM image for AlN:Er (24)...76
Figure 4-30. SEM image for AlN:Er (28)...77
Figure 4-31. SEM image for AlN:Er (32)...77
Figure 4-32. 5x5um2 AFM image for AlN:Er (20). 79
Figure 4-33. 5x5um2 AFM image for AlN:Er (24). 79
Figure 4-34. 5x5um2 AFM image for AlN:Er (28). 80
Figure 4-35. 5x5um2 AFM image for AlN:Er (32). 80
Figure 4-36. PL scan of Er emission at 1540 nm for AlN:Er (20)..................................82
Figure 4-37. PL scan of Er emission at 1540 nm for AlN:Er (24)..................................82
Figure 4-38. PL scan of Er emission at 1540 nm for AlN:Er (28)..................................83
Figure 4-39. PL scan of Er emission at 1540 nm for AlN:Er (32)..................................83
Figure 4-40. PL scan of Er emission overlay at 1540 nm for all AlN:Er samples. 84

CHAPTER 1: INTRODUCTION

Erbium is one of the Rare Earth (RE) elements and it is characterized by the partially filled 4f electron shells and their intrinsic spectral emission. This emission is not affected by the surrounding atoms as the 4f energy levels are relatively shielded by 4p and 5p electron shells. Erbium (Er) has an electronic transition from energy level $^4I_{13/2}$ to $^4I_{15/2}$ which results in an interesting 1.54µm emission that falls in the minimum spectral optical loss in modern optical silica fibers used in telecommunications [1-6].

III-Nitride materials have been viewed as appealing host semiconductor candidates for high efficiency Er doping in optoelectronic applications. This is due to their physical and chemical properties such as direct and wide bandgap, strong chemical bonds, high mechanical hardness, high melting point and high thermal conductivity. On the other hand, much effort has been done to explore Er doped III-Nitride materials for high emission intensity and it is demonstrated that Er emission intensity at 1.54µm in semiconductors (as host materials) deceases substantially from very low temperature (close to 0°K) to room temperature, this phenomena is known as Thermal Quenching effect. It was well demonstrated that this effect depends on the host material bandgap. It is predominant for small bandgap semiconductors while it is less effective in large bandgap semiconductors [7-10].

It has been demonstrated that the thermal quenching for Er emission intensity at 1.54µm is substantially lower in Gallium Nitride (GaN) (E_g = 3.4 eV) as host material comparing to other smaller bandgap semiconductors such as Silicon (Si) (E_g = 1.12eV)

and Gallium Arsenide (GaAs) (Eg = 1.43eV) which was reported by C. Ugolini et al. [7,8]. Furthermore, it was reported by T. T.M. Altahtamouni et al. that, at room temperature, Er emission intensity using Aluminium Nitride (AlN) (Eg = 6.1 eV) as host material is higher than GaN [11].

AlN is a III-Nitride material that has attracted a significant scientific interest due to its wide bandgap of 6.1 eV as well as the appealing properties as III-N material. AlN material has many applications such as deep Ultra Violet (DUV) optoelectronics, microelectronics operating at elevated temperatures, optical devices coating and sensing devices. [12-14].

AlN as host material for Er has been investigated by several research groups using different techniques for synthesis such as Ion Implantation [15] and Radio-Frequency Magnetron Sputtering [16]. Thus far, there was only one report about Er doped AlN (AlN:Er) synthetized using MOCVD growth technique. In that report, the Er emission at 1.54 μm showed a larger intensity and less thermal quenching comparing to Er-doped GaN. The report studied the effect of the growth temperature on the optical and structural properties of AlN:Er [11]. However, as yet there is no report about Erbium flux effect on AlN:Er.

In this thesis, we study the effects of Er flow rate on the structural and optical properties of AlN:Er grown by MOCVD. This thesis is represented mainly in five chapters. The first chapter is this introduction. The second chapter consists of a literature review on the previous efforts done on Er doped materials. The third chapter is dedicated

to describe the experimental tools and set-ups for Er-doped AlN growth, advanced imaging, surface analysis and material characterization. These techniques are Metal Organic Chemical Vapor Deposition, X-ray Diffraction, Photoluminescence Spectroscopy, Surface Analysis and Advanced Imaging Microscopy. The fourth chapter consists of presenting and discussing the results. The final chapter will be the conclusion of this thesis.

CHAPTER 2: LITERATURE REVIEW

1. III-Nitride Materials

III-Nitrides (III-N) namely the binary compound InN, GaN, AlN as well as the ternary and quaternary compounds such as AlGaN and AlGaInN are part of III-V materials as shown in figure 2-1; III-N are distinguished by their direct bandgap which varies from 0.7 (InN) to 6.2eV (AlN) and these materials can be used for optoelectronic devices due to their tunable optical emission which varies from the infrared to deep UV range as illustrated in figure 2-2. These materials have the n-type and p- type doping capability represented in figure 2-3 using Aluminium Nitride (AlN) as an example. III-Ns are characterized as well by their strong covalent chemical bonds which protect the materials from rough atmospheres [17]. They are known with their high mechanical hardness as well as their high thermal conductivity that allows the dissipation of the heat outside the material when used at high temperature [18-21].

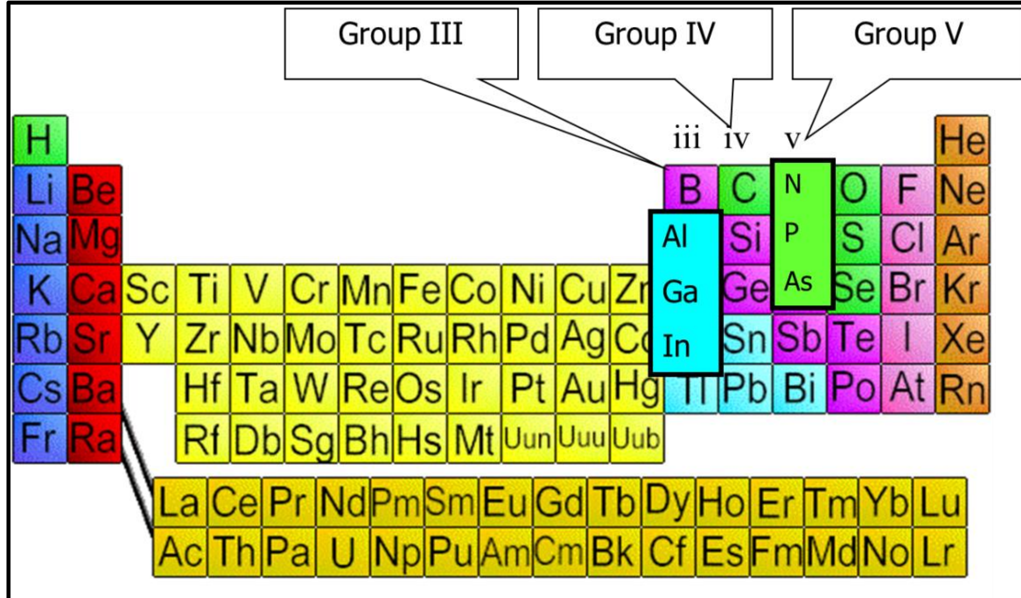

Figure 2-1. Chemical elements in III-V compound semiconductors (Chemical Elements.com 2014).

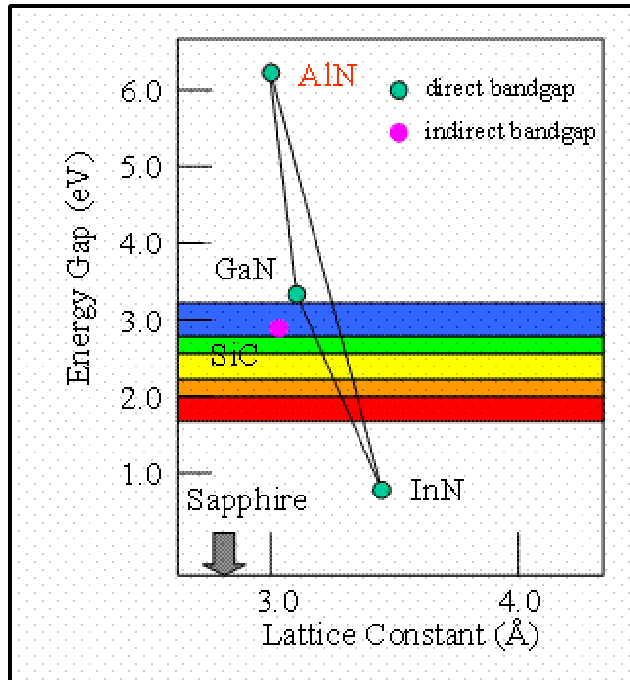

Figure 2-2. Band-gap and lattice parameter for III-Nitride materials (Nanophotonics Center @ TTU 2010).

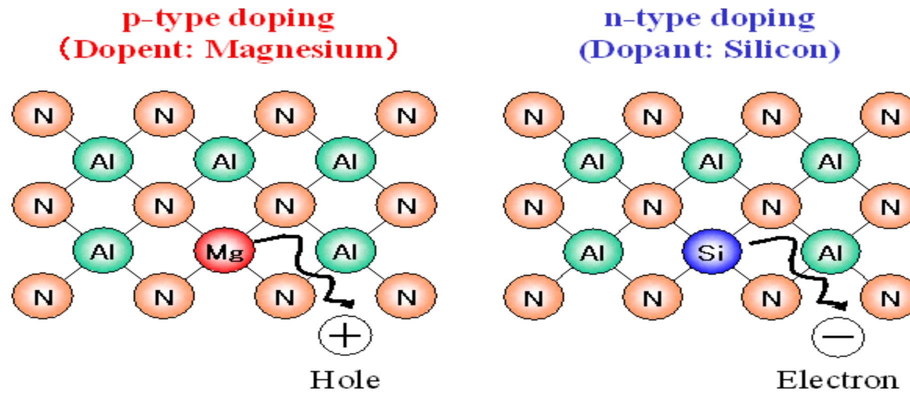

Figure 2-3. n-type and p-type AlN (Luger Research e.U. Institute for Innovation and Technology 2017).

The bandgap is the required minimum energy for an electron to move from the valence band to the conduction band, which is the energy difference between the highest energy of the valence band and the lowest energy of the conduction band. In semiconductors, there are materials which exhibit a direct bandgap such as III-Nitrides and others known as indirect bandgap materials namely SiC, GaP, AlP. Figure 2-4 shows the difference between the direct and indirect bandgap. In direct bandgap semiconductors, the electron transition from the conduction band to valence band takes place without change in momentum, so all the bandgap energy is converted into a photon as per the energy conservation principle. While in case of an indirect bandgap, this transition is always associated with a change of momentum. As result, part of the bandgap energy will be converted into a phonon (quantum of energy related lattice vibration in the crystal). For optoelectronic application, it is essential to use direct bandgap materials for high emission intensity.

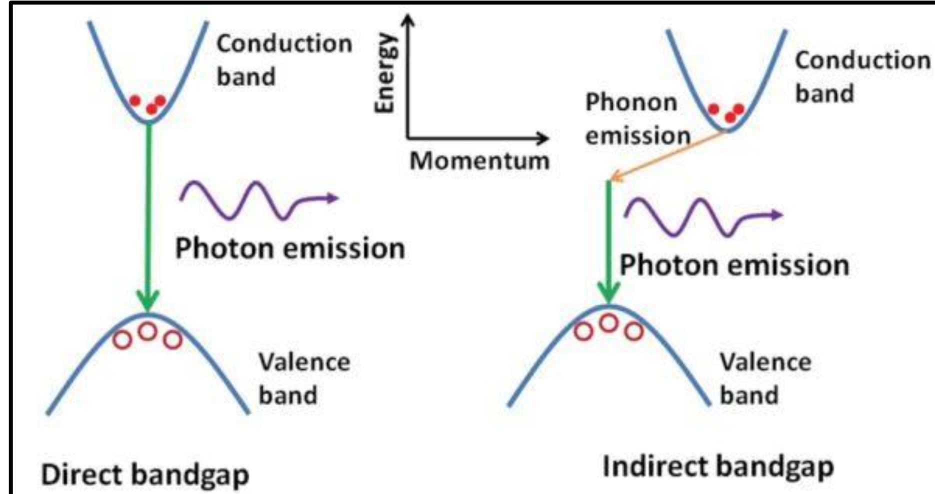

Figure 2-4: Photon emission process – direct and indirect band gap (Greg Sun - Advances in Optics and Photonics 3, 53–87 (2011)).

III-N materials are investigated widely in optoelectronics for Light-Emitting Diodes (LEDs) and Laser Diodes (LDs) in order to enhance the performance of these devices. N-III ternary and quaternary alloys are miscible which make the growth of hetero-structures possible using state of art deposition techniques.

2. III-Nitrides chronological development

The first report about GaN synthesis was in early 1930's, it was synthesized by flowing ammonia on the gallium surface at high temperature, this method was used by many research groups to prepare GaN platelets as well as needles in order to study the crystalline and optical properties of GaN. The breakthrough of GaN synthesis took place at the end of the 1960's using relatively advanced techniques for epitaxial growth of GaN on Sapphire substrate [22-24]. The growth conditions were not controlled efficiently which did not enable high quality un-doped GaN; the synthetized GaN materials were

mostly n-doped exhibiting electron concentrations between 10^{18} and 10^{20} cm^{-3}. In order to synthetize p-type GaN, certain elements like Mg and Zn were introduced to GaN in the growth process. Other techniques were employed to dope the synthetized GaN (after the growth) such as ion implantation [25-29].

Since the 1990's, major developments took place in growth techniques especially for Metalorganic Chemical Vapor Deposition (MOCVD) and Molecular Beam Epitaxy (MBE), the growth conditions were controlled more efficiently which enabled the high purity growth and low background defects due to contamination. This major development enabled the growth of InN and GaN for high performance optoelectronic devices [30-33].

3. Aluminium Nitride (AlN) crystalline properties

AlN is a very interesting III-Nitride binary compound as it consists of two very abundant chemical elements namely aluminium and nitrogen. As shown in figure 2-5, AlN has a hexagonal wurtzite crystal structure in its most stable crystal form. The two atoms (Al and N) occupy two sub-lattices in the hexagonal close packed (HCP) system. Each atom (e.g. N) shares covalent bonds with four other kind atoms (e.g. Al). This crystal structure can be represented as stacks of ABABAB planes of Nitrogen (A) and Aluminium (B) atoms (figure 2-5) and as tetrahedral units of [AlN_4] stacked along c direction as illustrated in figure 2-6. Hexagonal wurtzite AlN structure is characterized by the space group $P6_3mc$(186), its cell parameters are a = 0.311nm and c = 0.4982nm as shown in Table 2-1. The cell parameters "a" and "c" can slightly vary in scientific reports [34,35].

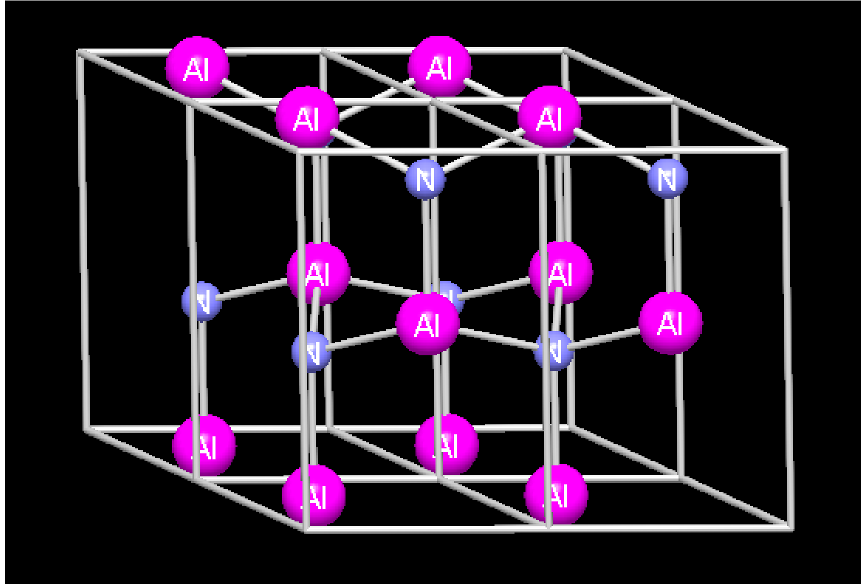

Figure 2-5. Aluminum Nitride Wurtzite structure.

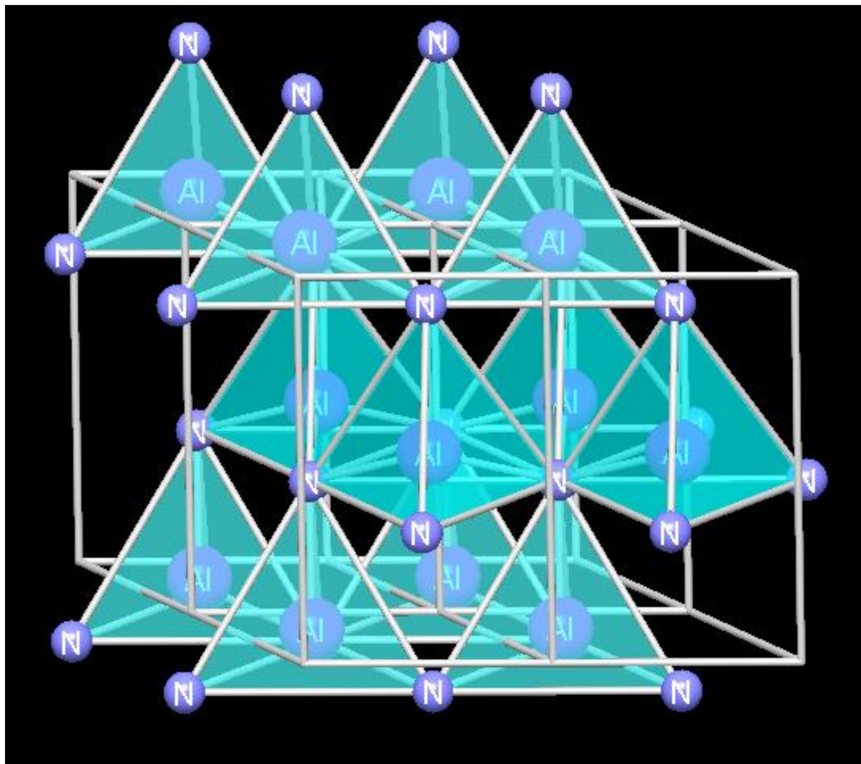

Figure 2-6. Aluminium Nitride structure represented as tetrahedral units of [AlN4].

Table 2-1. Standardized crystallographic data.

Space group	$P6_3mc$ (186)							
Cell parameters	a = 0.311, b = 0.311, c = 0.4982 nm, α = 90, β = 90, γ = 120° V = 0.04173 nm^3, a/b = 1.000, b/c = 0.624, c/a = 1.602							
Atom coordinates	**Site**	**Elements**	**Wyck.**	**Sym.**	***x***	***y***	***Z***	**SOF**
	N1	N	2b	3m.	1/3	2/3	0.0	
	Al1	Al	2b	3m.	1/3	2/3	0.381	

AlN wurtzite structure possesses many diffraction planes such as (100), (002), (101); previous studies have determined the inter-planar spacing of these diffraction planes which is already available in X-ray diffraction (XRD) databases. For AlN powder or thin film, the inter-planar spacing of the diffraction planes can be determined experimentally using XRD systems. Figure 2-7 shows an example of x-ray diffraction pattern of AlN powder where the positions of the peaks are characteristic to the diffraction planes in the AlN structure as indexed in this figure [34].

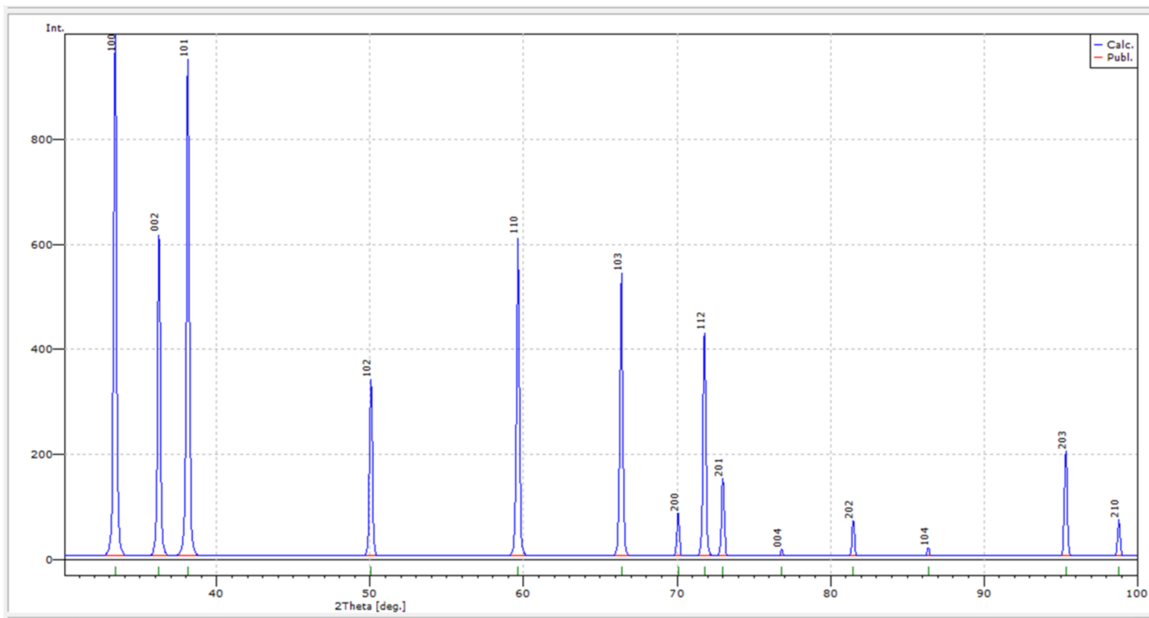

Figure 2-7. Powder X-ray Diffraction for AlN.

4. Thermodynamic and chemical properties of AlN

AlN is chemically stable at high temperatures in absence of corrosive environment. Its melting point is above 2000°C which makes it suitable for high temperature operations. The thermal conductivity of AlN is 2.85 W $cm^{-1}°C^{-1}$ at room temperature which is higher than InN and GaN. However, its thermal conductivity is temperature dependent [36-38].

At room temperature, its linear thermal expansion coefficient is 5.3 x $10^{-6}°K^{-1}$ and its volumetric thermal expansion coefficient is $4.2x10^{-6}°K^{-1}$. AlN is highly stable at high temperature in inert atmosphere; however above 700 ^{0}C, a thin film layer of 5 to 10 nm of Aluminium Oxide is formed in presence of oxygen. At higher temperature above 1400^{0}C (which is close to the melting point of the Aluminium Oxide) the oxidation gets through the oxide layer and the material can be damaged completely [35,39].

A surface analysis performed by X-ray Photoelectron Spectroscopy combined with depth profiling on AlN surface by Slack and McNelly [40] reported that the thickness of an oxide passive layer is between 5 to 10 nm, this layer was formed in presence of oxygen while exposed to air; it acts as a barrier and prevent further contact and reaction between the oxygen and the Aluminium Nitride. Many research groups investigated the chemical stability of AlN thin films using different methods of etching and reported that AlN material could withstand many types of etching especially at room temperature [36].

5. Mechanical properties of AlN

Aluminum Nitride is a hard ceramic material due to its strong covalent chemical bonds between the Aluminum and Nitrogen atoms. AlN single crystal exhibits a high mechanical hardness along the c-plane (the basal plane of (0001)) which is to be around 12GPa while the hardness along the axis perpendicular to the c-direction varies between 10 and 14 GPa. It was reported that the bulk modulus of single crystal AlN varies between 160 GPa and 201 GPa and Young's modulus is at the range of 193 ~ 208 GPa. This was determined using Surface Acoustic Wave (SAW) which is a technique that uses acoustic waves along the material surface to probe the mechanical strain of material [35,39,41,42].

6. Band structure and electrical properties of AlN

Band structure studies for semiconductors are important in order to classify the materials and consider their candidate applications. For AlN as well as III-N materials in general, several researcher groups were investigating of these materials and working on band-structure calculations for namely AlN wurtzite. AlN is a wide direct bandgap semiconductor and figure 2-8 shows its band structure at 300°K. As it is illustrated in the band structure, the bandgap energy which is the energy difference between the highest point of the valence band and the lowest point of the conduction band is equal to 6.2 eV [43].

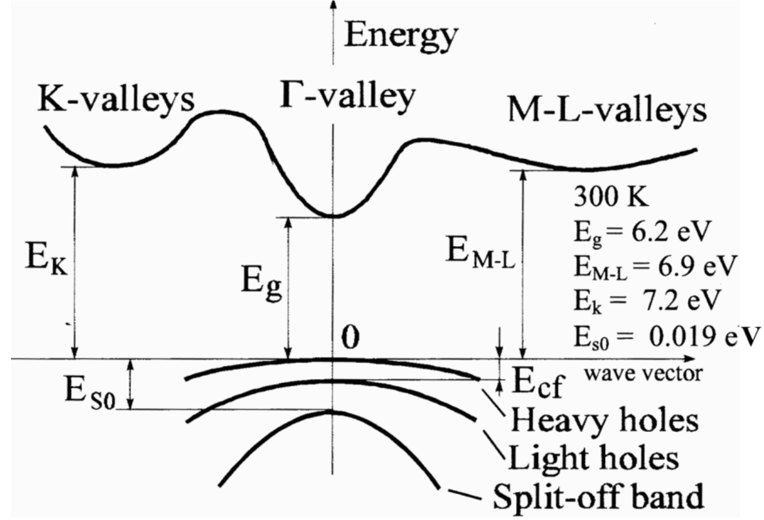

Figure 2-8. Bandgap structure of wurtzite AlN.

AlN has a high resistivity which was reported between 10^{11} and 10^{13} Ω.cm which is related to the low intrinsic carrier concentration, as well as the energy levels of impurities introduced to the material and the deep-level traps (defects). The intrinsic carrier concentration is the concentration of the charge carriers present in the un-doped semiconductor material. The concentration of these charge carriers is crucial for the conductivity and depends on the bandgap and the temperature [35,39,41,44].

7. Rare earth doped semiconductors

Semiconductors doped with rare earth (RE) elements have attracted a lot of interest for their unique optical properties. A.R. Zanata was the first to report photoluminescence emission of Er doped SiN in 1998 and shortly afterwards Steckl achieved Er doped GaN device with PL emission in the visible range [45,46].

RE elements have $[Xe]5s^24f^n$ electronic configuration where the 4f electron shell

inside the 5s5p ones. The host semiconductor has almost no effect on the 4f electrons as they are shielded by 5s5p shells and their energy levels are almost unaffected. In RE elements, electrons have different possible transitions between 4f energy levels which provide different emission lines from UV to Infrared as illustrated in figure 2-9.

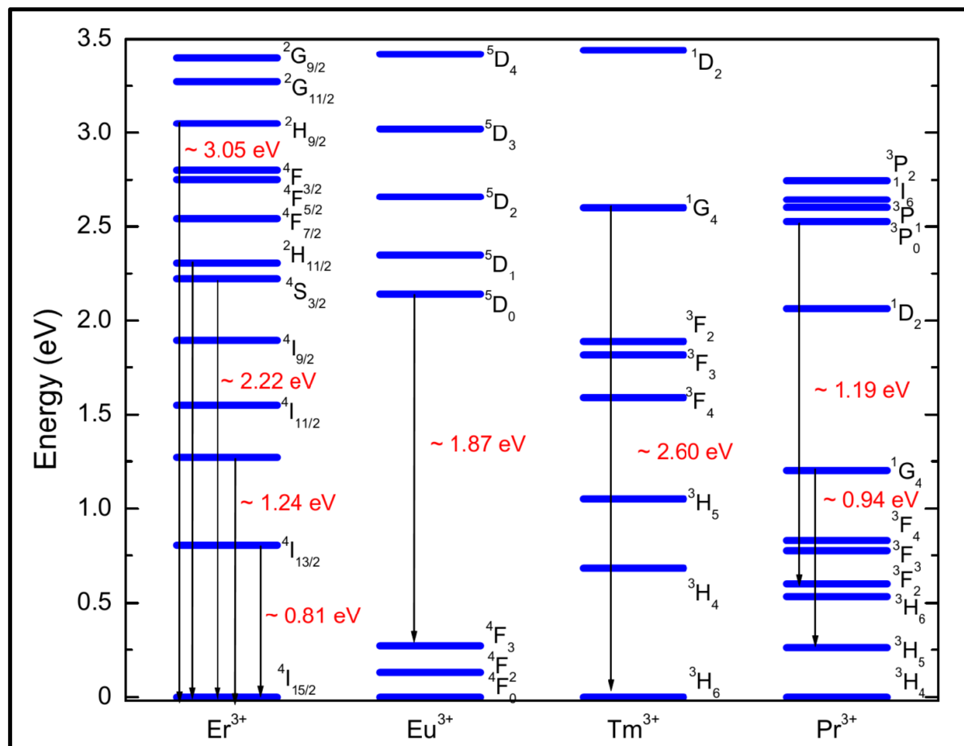

Figure 2-9. Energy level chart of certain trivalent rare earth elements (Er3+, Eu3+, Tm3+, Pr^{3+}) in GaN (I-Wen Feng 2013).

Using RE as doping elements in III-Nitride materials for optoelectronic applications provides characteristic emissions which are intrinsic to the RE and relatively independent of the III-N host and temperature. In operation, the semiconductor host excites the trivalent RE ions specifically intra-4f shell electrons and the transition of electrons to their lower energy levels is accompanied by characteristic

emissions (figure 2-9).

8. Erbium doped semiconductors

Nowadays, telecommunication plays a major role in the global development. Internet relays remarkably on the fiber optics that has specific optical properties namely the optical loss which is illustrated in figure 2-10. In 1980s, fibers used to have major optical loss mainly in two regions between 900 - 1000 nm and 1300 - 1450 nm. However, for the modern fibers the lowest lost region is between 1450 - 1650 nm. In the other hand, Erbium has a characteristic emission of 1540 nm which corresponds to the minimum optical loss range for modern fibers [1-6]. This has enabled the implementation of the Erbium in optical devices such as Erbium-doped fiber amplifier EDFA shown in figure 2-11, which is widely used to amplify the optical signal intensity through fiber optics. Its basic principle is shown in figure 2-12.

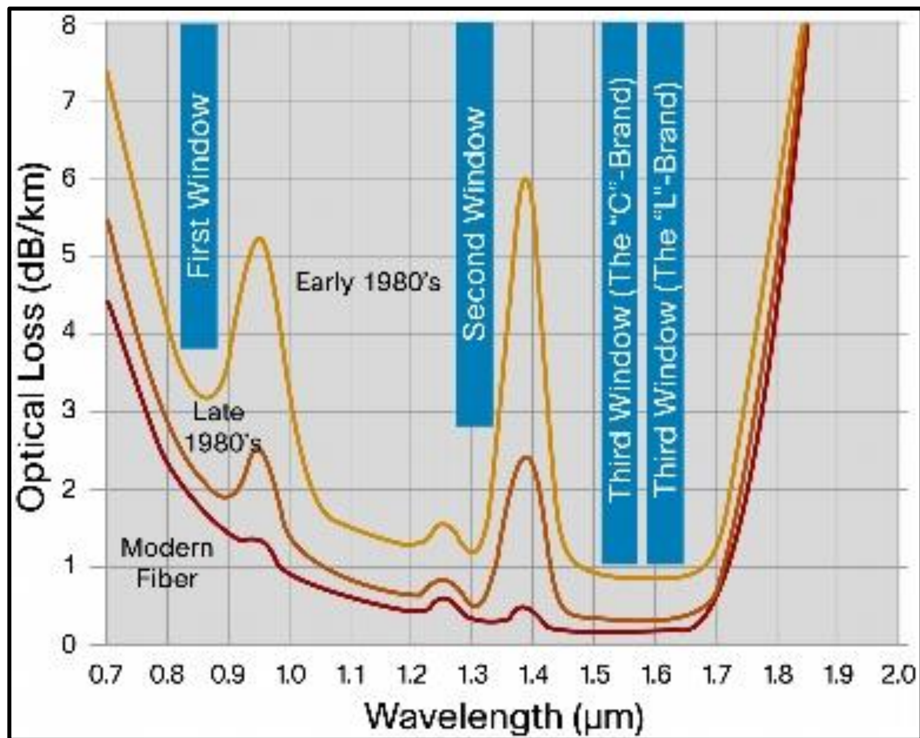

Figure 2-10. Optical loss for optical fibers as a function of signal wavelength (White Paper - Fiber Types in Gigabit Optical Communications 2008).

Figure 2-11. Erbium Doped Fiber Amplifier device (Finisar Corporation 2016).

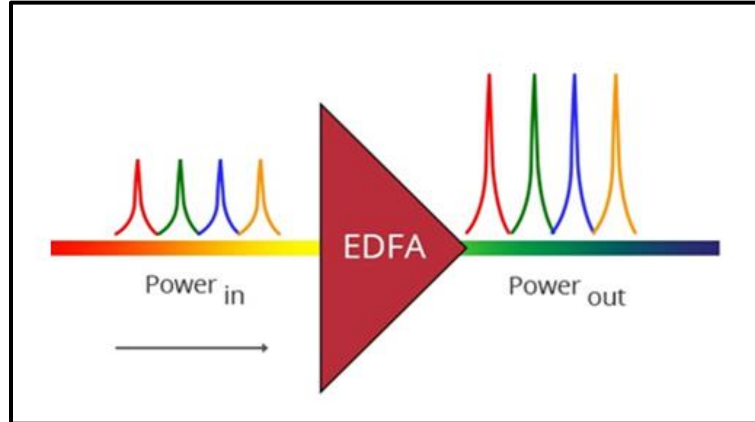

Figure 2-12. Erbium Doped Fiber Amplifier basic principle (FS.COM 2017).

The trivalent ion Er^{3+} has characteristic emission lines in the visible and infrared range. The most interesting transition for fiber optics in telecommunication is the one from the energy level $^4I_{13/2}$ to the energy level $^4I_{15/2}$ which results in the emission at 1.54 µm as shown in figure 2-13.

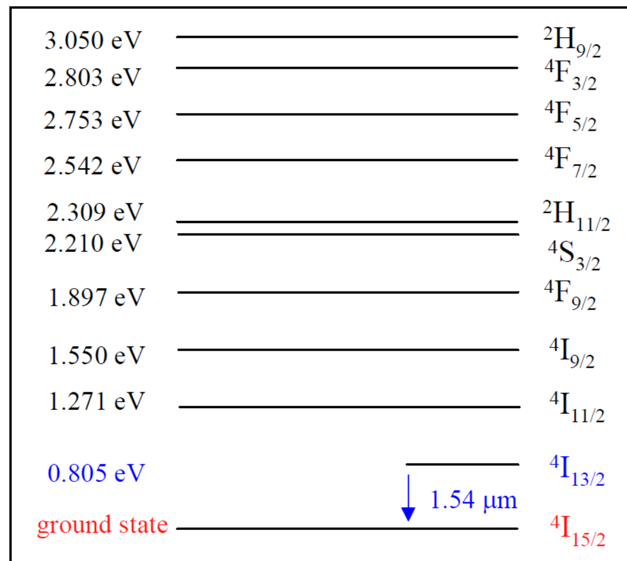

Figure 2-13. Energy levels of the trivalent Er^{3+} 4f electrons at 1.54 µm (Cristofer Ugolini 2008).

Figure 2-14 shows the Photoluminescence (PL) intensity measurements of 1.54 μm peak for Er^{3+} optical emission as a function of temperature in different host materials, Er was implanted in different host materials at room temperature using high energy Er^{+} ions of E=330KeV, the dose slightly varied between 10^{13} and 10^{14} Er^{+} cm^{-2} and the samples were annealed afterwards using rapid thermal annealing. As shown in the figure, Er^{3+} PL emission (at 1.54 μm) intensity in different semiconductors (as host materials) as a function of temperature. It is clearly observed that semiconductors with smaller bandgaps undergo a substantial intensity reduction for Er related emission at 1.54 μm from low temperature (close to 0°K) to room temperature. This intensity reduction is known as thermal quenching.

Thermal quenching is predominant in smaller energy bandgap (E_g) host semiconductors such as $Ga_{0.38}In_{0.62}As_{0.84}P_{0.12}$ (E_g = 0.807eV) and it is less effective for higher bandgap materials such as CdS (E_g = 2.42eV). These experimental results support the direct relationship between bandgap and the thermal quenching and suggest that wider energy bandgap host materials provide lower thermal quenching [10].

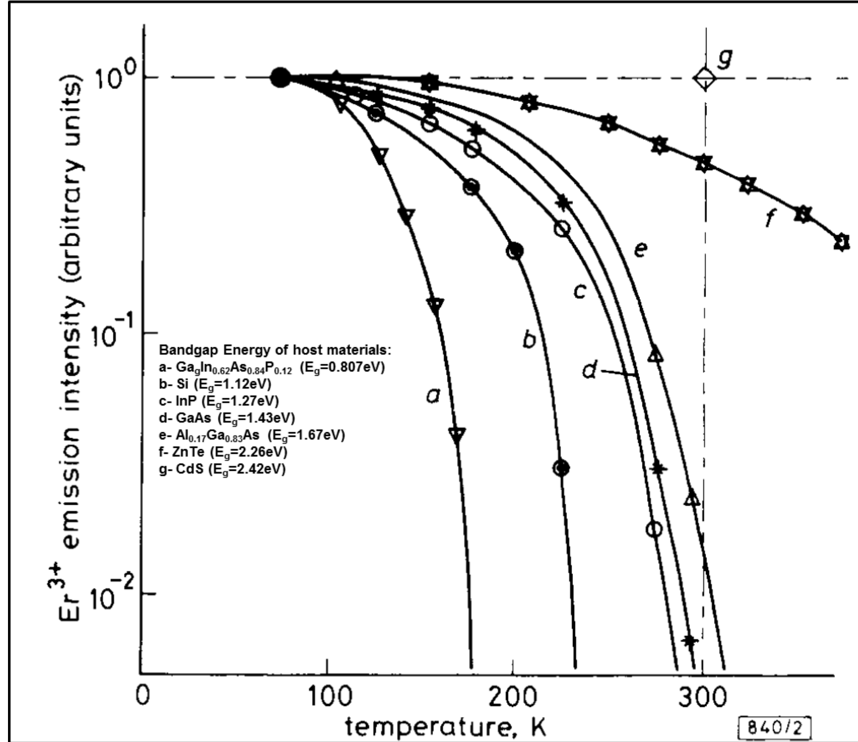

Figure 2-14. Er^{3+} emission in different host materials in different temperatures.

C. Ugolini et al. reported thermal quenching of 20% between 10 and 300°K using Er-doped GaN epilayers which is significantly smaller thermal quenching than other narrower bandgap host materials [8]. T.M. Altahtamouni et al. reported higher Erbium emission intensity at 1.54 μm using AlN as host material compared to GaN and lower thermal quenching for AlN:Er of factor 1.2 only between 10 and 300°K [11].

9. Erbium doped AlN

Synthesis of Er-doped AlN material was the center of interest for several research groups using different deposition techniques. R.G. Wilson et al. reported PL emission of trivalent Erbium ions at 1.54 μm for AlN:Er synthetized using ion implantation technique

[15]. F.S. Liu et al. reported the growth of c-axis oriented wurtzite structure Er:AlN films using Radio Frequency (RF) – Magnetron Sputtering in different conditions and found that using higher power, for sputtering, increases the PL intensity 1.54 µm and the grain size and lower the strain [16]. T.M. Altahtamouni reported high crystalline quality c-plane AlN:Er grown on c-plane sapphire using the state-of-art MOCVD and growth temperature effect on the 1.54 µm PL intensity and emission shape [11]. However, there is no report about the effects of Er flux on AlN:Er properties grown by MOCVD thus far and this study will be the main topic of this thesis.

Sapphire has a hexagonal sapphire structure and figure 2-15 shows sapphire unit cell. The lattice mismatch between sapphire c-plane and AlN c-plane is relatively small which enables the implementation of c-plane single crystal sapphire as a substrate for MOCVD grown c-plane AlN as shown in figure 2-16.

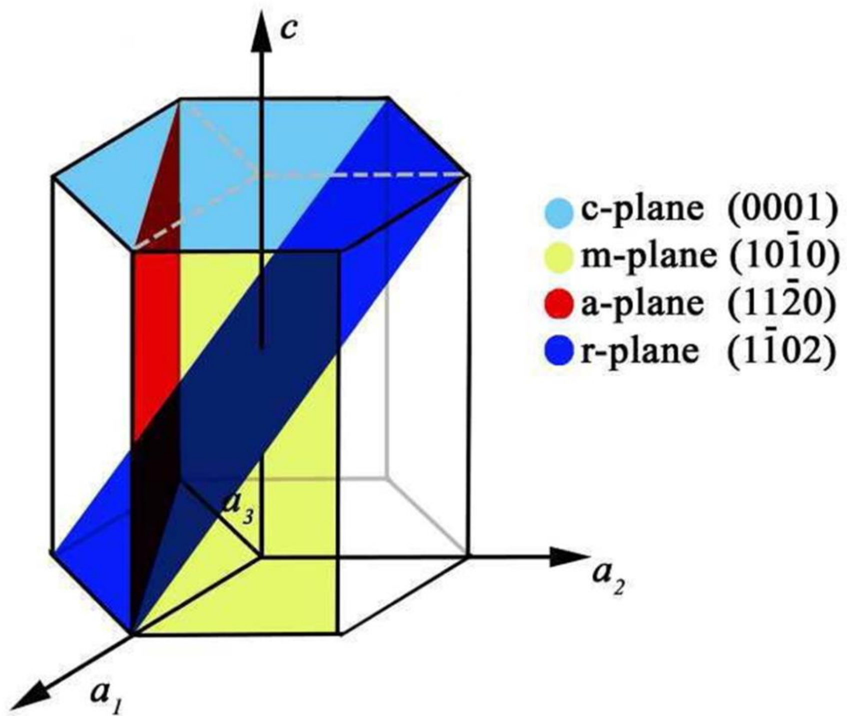

Figure 2-15: Sapphire unit cell (F. Cuccureddu et al, Surface Science 2010).

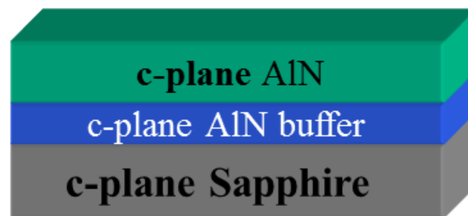

Figure 2-16: c-plane AlN on c-plane Sapphire.

CHAPTER 3: EXPERIMENTAL TECHNIQUES

1. Metalorganic Chemical Vapor Deposition (MOCVD)

MOCVD or sometimes called Organometallic Vapor Phase Epitaxy (OMVPE) is an advanced chemical vapor deposition technique; it is mainly used to grow compound semiconductors with highly advanced precision up to atomic layer. In the epitaxial growth, precursors are used to carry the target elements to the substrate as shown in figure 3-1. This technique provides one of the highest crystalline quality growths. Many compound semiconductor materials can be grown by MOCVD namely III-V materials which is composed of an element from group III (such as Al, Ga, In) and an element from group V (such as N, P, As). In this technique, the chemical reaction between the precursors takes place at the substrate where the temperature is controlled (usually fixed at high temperature) to enable the growth of the compound semiconductor. However, there are many factors involved in this process such as precursor's composition, temperature, pressure, substrate, etc. Substrate choice is important especially taking into consideration the lattice mismatch, thermal dilatation coefficient. Moreover, it is important to choose the right precursors to avoid any incompatibility or secondary phase formation. The chamber conditions also need to be optimized such as pressure, temperature and gas flow [47].

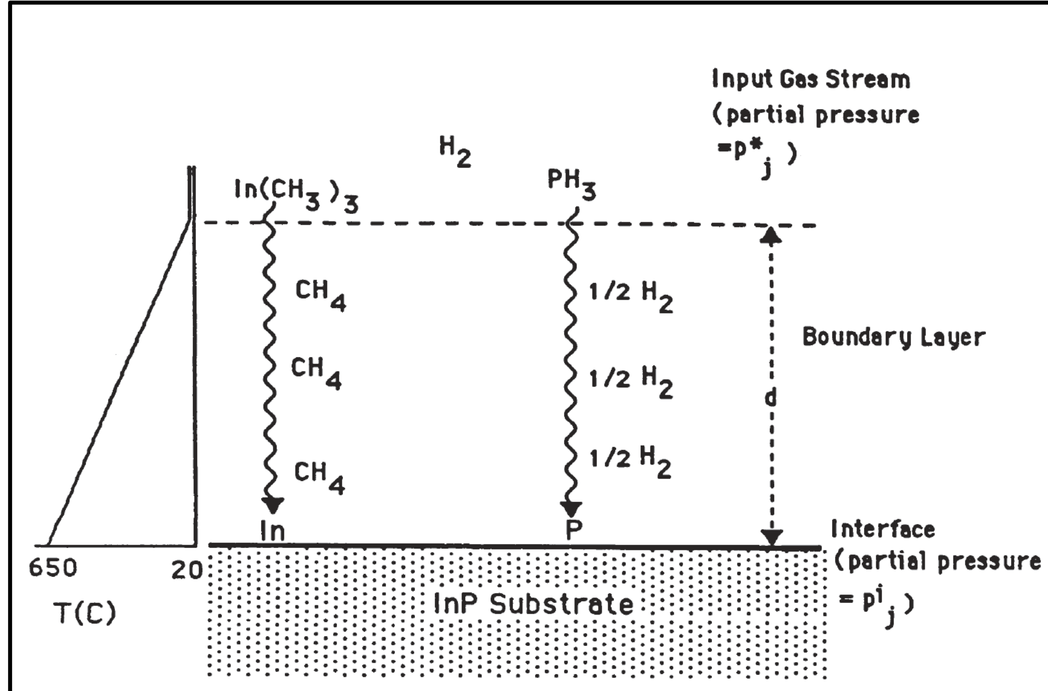

Figure 3-1. Example of InP MOCVD growth schematic using TMIn and PH3 precursors.

The precursors usually used in III-V growth by MOCVD are molecules that contain the target elements (Al, Ga…) attached with radicals such as methyl, ethyl. Trimethylaluminium $Al_2(CH_3)_6$ is an example of precursor that is used for AlN compound semiconductor growth. Technically, MOCVD consists of four key components. The first component is the gas supply and metal-organic sources control where the conditioning of the precursor bubblers takes place to convert the metal-organic sources (liquid or solid) into vapor state flow controlled by mass flow-meters. The second component is the reactor chamber where the conditions are controlled as per the required growth; the wall temperature must be kept cooler to avoid any pyrolysis reaction outside the substrate surface. The third component is substrate holder module; it controls the temperature of the substrate to enable the pyrolysis reaction within the

substrate surface. The last part is the pressure control and exhaust, where the pumping is controlled to maintain a constant low pressure inside the reactor. This part also controls the exhaust operations, the latter is important for the safety aspect, as the gases used in MOCVD are usually toxic and highly flammable. Figure 3-2 shows the diagram of MOCVD main components.

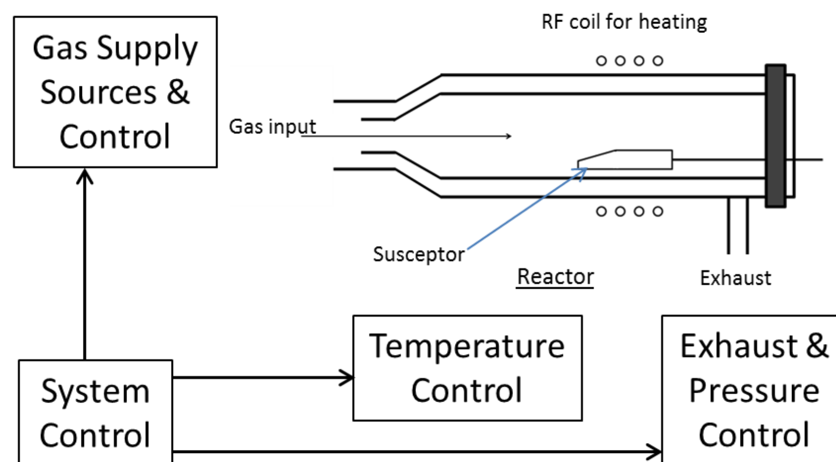

Figure 3-2. Diagram for MOCVD main components.

The substrate plays a major role in the crystal growth and the first few atomic layers at the interface are crucial for the stability of the growth, the lattice mismatch between the substrate and the grown crystal is reported to be a source of mechanical, electrical and optical issues; the lattice matching is important for device quality crystal growth. Commercial single crystal substrates are available in the market. However, their cost varies from affordable to very expensive. It is important to highlight that the cost of the process is crucial for up-scaling, so it is convenient to use affordable substrates.

MOCVD has been developed since early 1980's and nowadays it is considered as

a mature technique, there are many manufacturers for commercial MOCVD such as VEECO instruments. Figure 3-3 shows a photo of VEECO MOCVD system [48].

Figure 3-3. Image of MOCVD VEECO system.

2. X-ray Diffraction

X-ray diffraction (XRD) is one of the most important and useful characterization techniques. It gives information about material crystalline properties namely the crystalline structure, lattice constant, dislocation density and lattice strain. There are many kinds of XRD configuration such as Bragg Brentano measurement for bulk materials, four circles for single crystal and grazing incidence XRD for surface sensitive measurements mainly for thin films. XRD is a nondestructive technique consists of X-ray source, sample manipulator, goniometer (which controls the angles) and detector as shown in figures 3-4. The principle of XRD is based on Bragg's law which relates the x-rays wavelength, the lattice spacing of the crystal and the diffraction angle; so at Bragg conditions when x-rays scattered through the crystalline material, they interfere out of

certain crystalline planes in a certain direction which is the diffraction angle (angle between the incident x-rays and the scattered ones) as shown in figure 3-5.

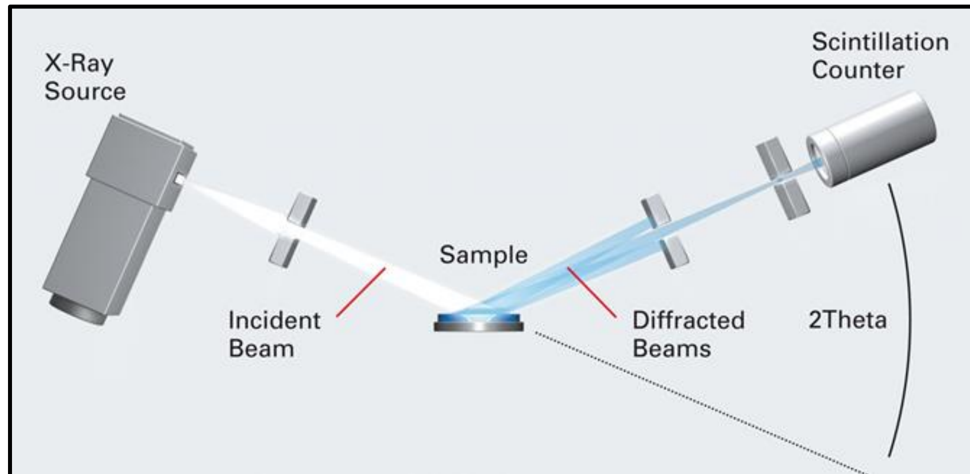

Figure 3-4. X-ray diffraction schematics (Bruker Corporation).

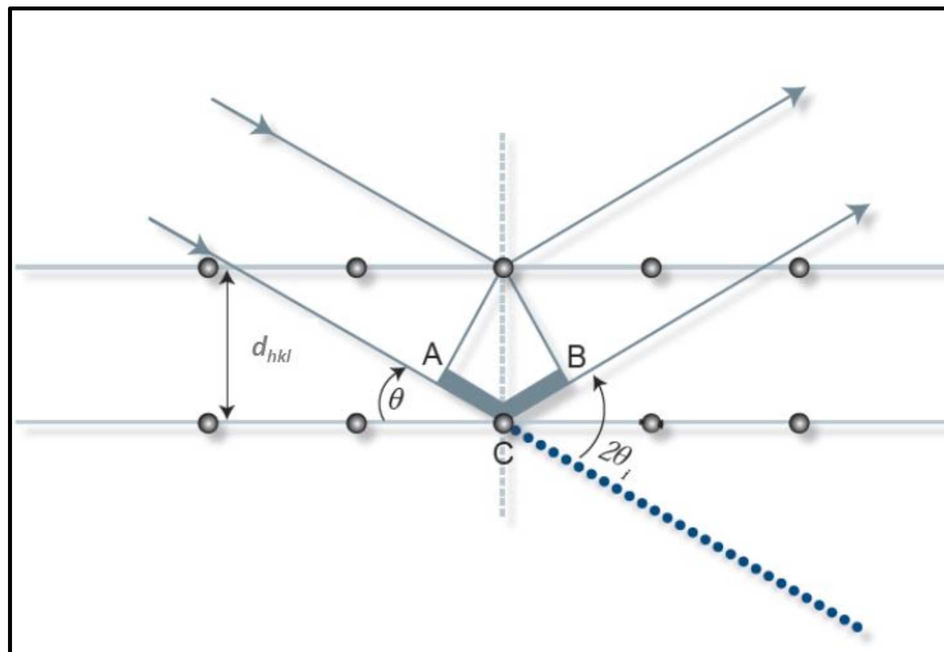

Figure 3-5. X-ray diffraction principle (Bruker Corporation).

Equation (3-1) is Bragg's relation, λ is the x-ray incident wavelength, d_{hkl} is

lattice spacing, hkl are Miller indices, θ is scattering angle and n is reflection order.

$$2d_{hkl}\sin\theta = n\lambda \qquad (3\text{-}1)$$

For AlN which has a hexagonal crystal structure with lattice parameters (a, c). The lattice spacing is expressed in equation (3-2).

$$d_{hkl} = \frac{1}{\sqrt{\frac{4}{3}\left(\frac{h^2+hk+k^2}{a^2}\right)+\frac{l^2}{c^2}}} \qquad (3\text{-}2)$$

Rocking curve is XRD measurement essentially for epitaxial single crystal films, the x-ray tube and detectors are fixed at the diffraction angle while the sample is performing tilting in a small range. If the sample is perfect single crystal the rocking curve scan around the diffraction angle will be a sharp peak with a small Full Width at Half Maximum (FWHM). However, if the epitaxial single crystal has lower quality especially defects; the peak will be broader with high FWHM. The rocking curve gives information about the crystal defects, dislocation density, mis-orientation and other parameters [49].

The X-ray diffractometer used in this study is D8 Advance Bruker AXS (figure 3-6), the source is an x-ray tube having a Cu anode with a characteristic wavelength K_α = 1.54Å. The software used is Diffracplus for measurements, Diffracplus.Eva for data analysis and the data base to identify the phases [50].

Figure 3-6. X-ray diffraction equipment.

X-rays are usually produced under vacuum where free electrons are generated by a heated filament using a high current. Then these electrons are accelerated by high voltage toward a target (anode). The interactions between the electrons and the metallic anode generate X-ray; there are two kinds of x-ray, fluorescence radiation which is characteristic to the anode material and Bremsstrahlung continuous radiation that is related to the applied high voltage. Figures 3-7 represents the x-ray tube schematics and the process of the x-ray generation.

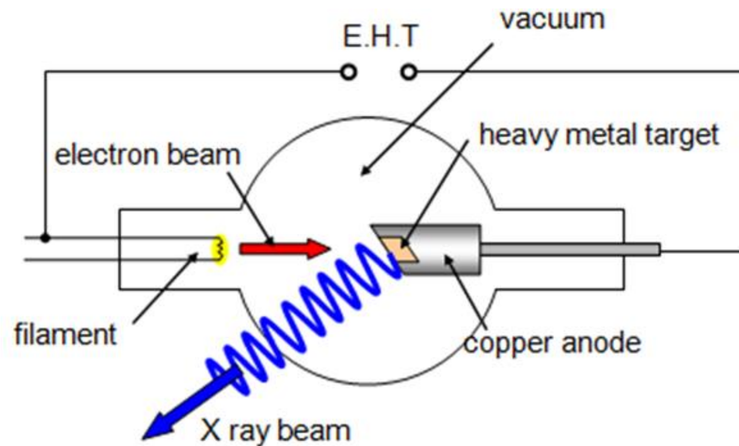

Figure 3-7. X-ray tube schematics (School Physics 2013).

3. Photoluminescence (PL) spectroscopy

Luminescence in general is the optical emission due to any physical or chemical phenomena except the blackbody radiation (radiation due to heat). An external excitation source is necessary for this process to take place. There are many luminescence processes such as Photoluminescence (PL), Electroluminescence (EL), Chemo-luminescence, Cathodo-luminescence (CL), etc. However, only the PL will be emphasized in this chapter. PL spectroscopy is a characterization technique which used to study the optical properties of the semiconductor materials, it is a nondestructive technique and it is involved in many research applications especially optoelectronics and photovoltaic materials; it can provide information about the intrinsic optical properties of semiconductors as well as the impurities. Its basic principle consists of the material capability of absorbing photons and reemitting other lower energy photons.

Figure 3-8 shows the PL process where a valence electron absorbs an incident photon ($E_i = h\nu_i$) and moves to the conduction band. Then the relaxation step takes place,

where the electron and the hole (left in the valence band) move to lower energy level within the band by emitting a phonon. The recombination is the last step where the electron moves back to the valence band and recombines with hole. As per the energy conservation principle it emits a characteristic photon ($h\nu = E_g$) which corresponds to the bandgap energy of the material ($\Delta E = E_g = E_c - E_v$).

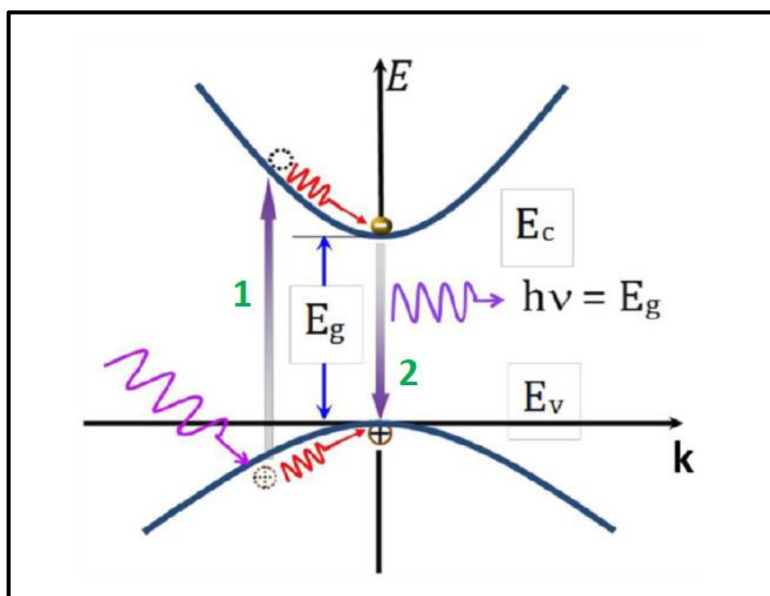

Figure 3-8. Energy diagram for photoluminescence process (Neeraj Nepal 2006).

The PL spectrometer consists mainly of a laser source as well as its related optics, sample stage, Monochromator which controls the selection of the wavelength and a detector. It measures the photoluminescence emission intensity as a function of the wavelength and it main application is in semiconductors. The sample preparation is not required which is one of the advantages of PL spectroscopy. Figure 3-9 shows the schematic of the main components of the PL spectrometer used in this thesis.

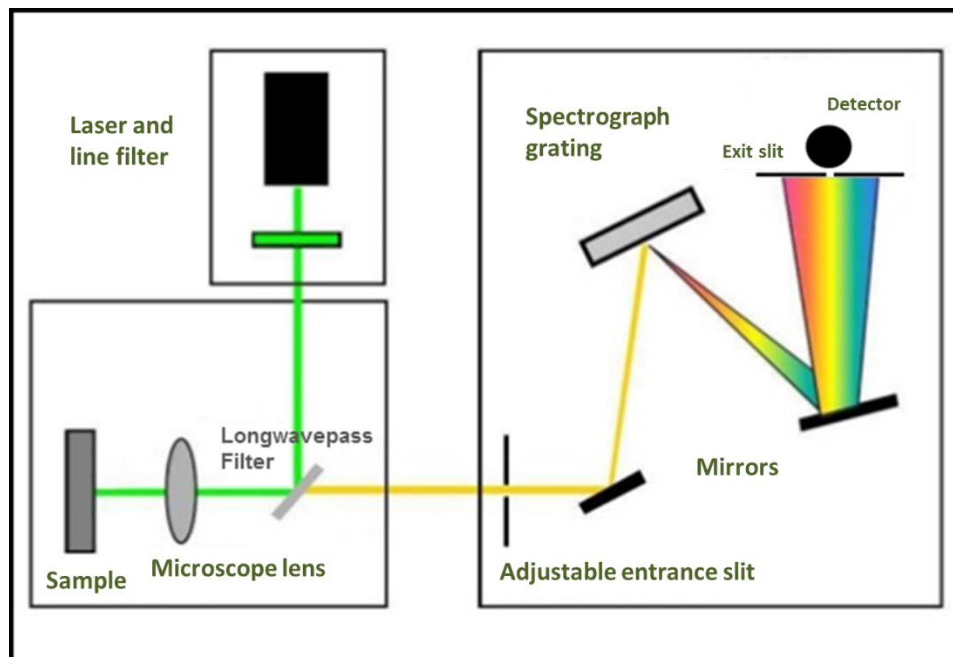

Figure 3-9. PL System schematics (David Lidzey 2016).

The system used for PL measurements is Maple II basic PL spectrometer from DongWoo as shown in figure 3-10, the spectral range was before from 539 to 900 nm based on the long-pass-filter, the photomultiplier detector and the laser source wavelength is 532 nm. As part of this thesis and in order to perform measurement in the infrared range up to 1700 nm, I upgraded the basic PL spectrometer by implementing modifications of hardware and software. This includes a new InGaAs detector with a detection range from 1000 to 1700nm from the manufacturer DongWoo and Longwavepass filter from Semrock that is transparent mainly in the IR range, as shown in figures 3-11 and 3-12 [51].

Figure 3-10. Schematic diagram of the PL spectrometer.

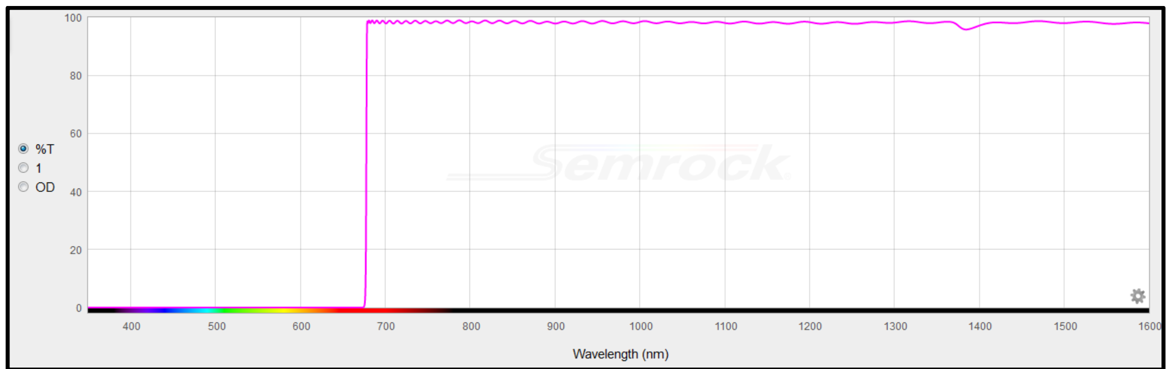

Figure 3-11. Longwavepass filter spectrum (Semrock 2016).

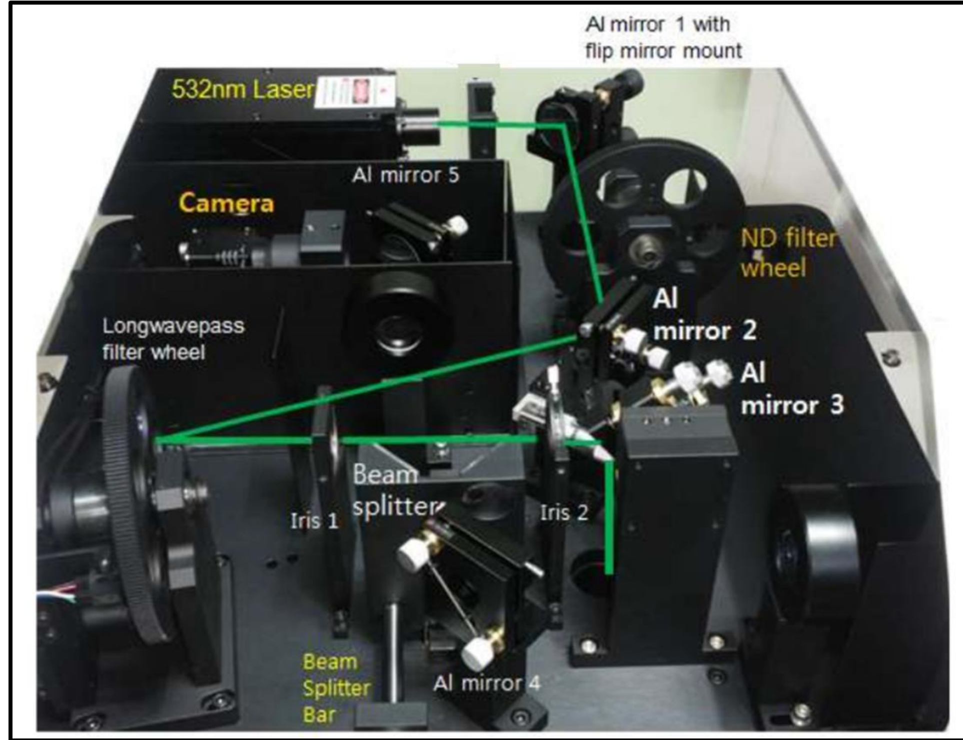

Figure 3-12. Top view of the optical path (DongWoo Optron 2014).

4. Surface Analysis

Surface science is a branch of science that focuses on the physical and chemical phenomena that takes place at the surface of materials and the interfaces between two layers. It is involved in many aspects of our lives namely battery electrodes, airplane engine blade, microchips, hetero-junction solar cells, fuel cells, super-hydrophobic, self-cleaning coatings, etc. However, it is still a debate to how define the "Surface" thickness used in surface science. Generally, a bulk material has all dimensions above 1 µm, thin film is a material that has a thickness between 10 and 1000 nm and the ultra-thin film is between 1 and 10 nm and the "surface" is few atomic layers thickness which is up to 1nm. Surface analysis and characterization play a major role in surface science and most

of them require sophisticated sources, ultra-high vacuum (UHV) and specialized and sensitive spectrometers, which make them very expensive equipment that are available only in central laboratories.

There are many surface analysis techniques, few of them are relatively common, such as X-ray Photoelectron Spectroscopy (XPS) or sometimes called Electron Spectroscopy for Chemical Analysis (ESCA), Time of Flight Secondary Ion Mass Spectroscopy (TOF-SIMS), Auger Electron Spectroscopy (AES). All these techniques are involved in the surface science and provide complementary information. The diagram in figure 3-13 (from Evans group) shows different characteristic of these techniques such as the detection range, the analytical spot for many techniques including XPS, SEM, AFM and TOF-SIMS [52].

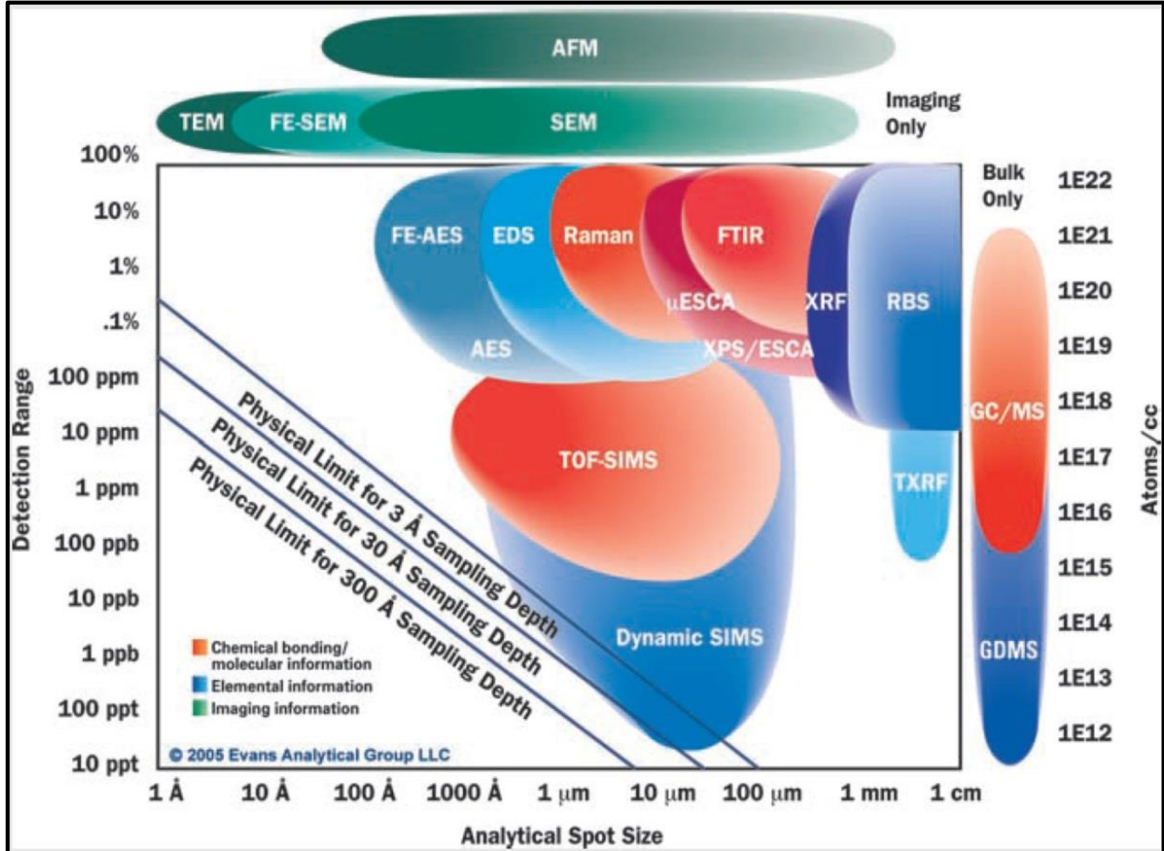

Figure 3-13. Analytical resolution & detection limit for the most common characterization tools (Evans Analytical Group LLC 2005).

a. X-ray Photoelectron Spectroscopy

XPS is a non-destructive analysis technique and gives information about the existing elements on the surface as well as their chemical state. It provides also the quantitative analysis and other information about the material surface combined with different sources or techniques such as UV Photoelectron Spectroscopy (UPS). XPS is surface sensitive technique which can detect effectively signals only up to approximately 5 nm depending mostly on photoelectron energy. Depth profiling technique using Argon

source for surface etching allows performing XPS measurement through depth, this technique is highly important for characterization of hetero junction thin films and interfaces.

As per Evans diagram in figure 3-13, XPS detection range for a reliable quantitative analysis is between 0.5 to 100% with an analysis area (spot size) from 3 µm up to hundreds of micrometers in diameter using monochromated x-ray source and up to millimeters using a direct source. The basic principle of XPS relies on the Photoelectric effect as shown in figure 3-14. The incident x-ray interacts with a core level electron; the energy of the x-ray photon is transferred to the electron. Part of this energy will be used to move the electron from it energy level to the fermi level, in other words to leave the atom, this required energy is known as the binding energy. The second part of the energy is used to carry the electron from the Fermi level to the vacuum level; this energy is required for the electron to leave the material surface which is known as the work function. The rest of the energy will be converted into kinetic energy for the electron as illustrated in figure 3-15.

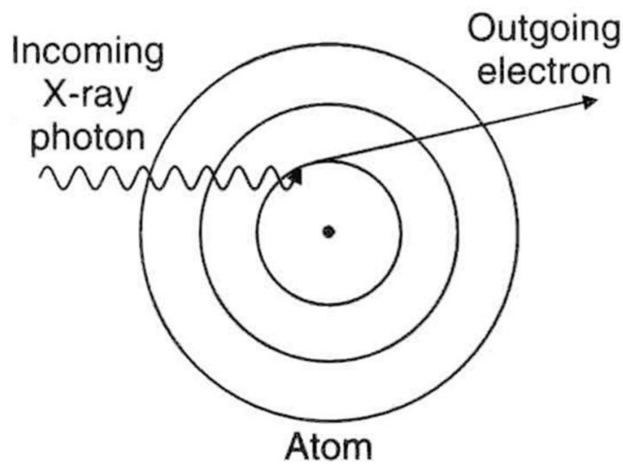

Figure 3-14. Schematic of photoelectric effect (University of Hang Kong 2011).

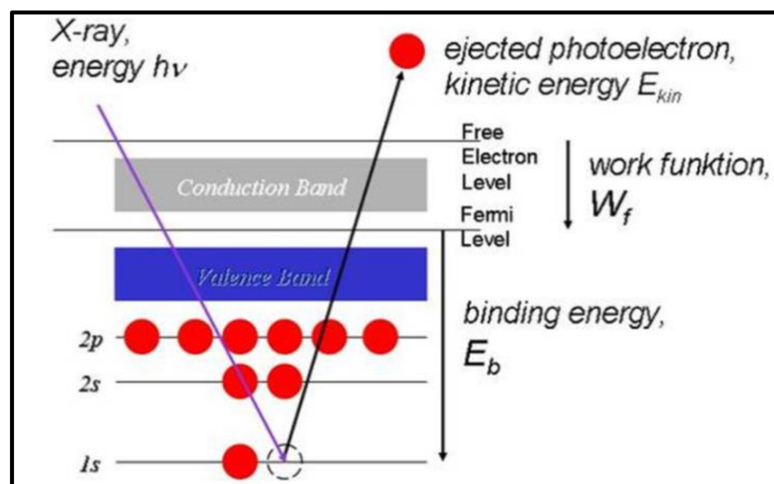

Figure 3-15. Schematic of electrons energy levels in photoelectric process (Leibniz Institute for Solid State and Materials Research Dresden).

As per the energy conservation principle, the energy of the x-ray photon is equal to the sum of the electron binding, work function and the kinetic energy of the ejected photoelectron as per the equation (3-3).

$$hv = E_b + W_f + E_{kin} \tag{3-3}$$

Where E_{kin} is the Kinetic energy of the electron, hv is the incident photon energy, E_b is the binding energy of an electron and W_f is the work function.

In X-ray Photoelectron Spectroscopy, the main objective is to measure the photoelectrons intensity as a function of binding energy. The spectrometer can measure the intensity of photoelectrons at each kinetic energy (normally it is a narrow pass energy). The photon energy of x-ray source is known and the work function of the spectrometer can be measured using a standard sample. So the binding energy can be calculated using equation (3-4).

$$E_b = hv - W_f - E_{kin} \tag{3-4}$$

Normally, the XPS spectrum is a graph of photoelectron intensity as a function of bonding energy as shown in figure 3-16.

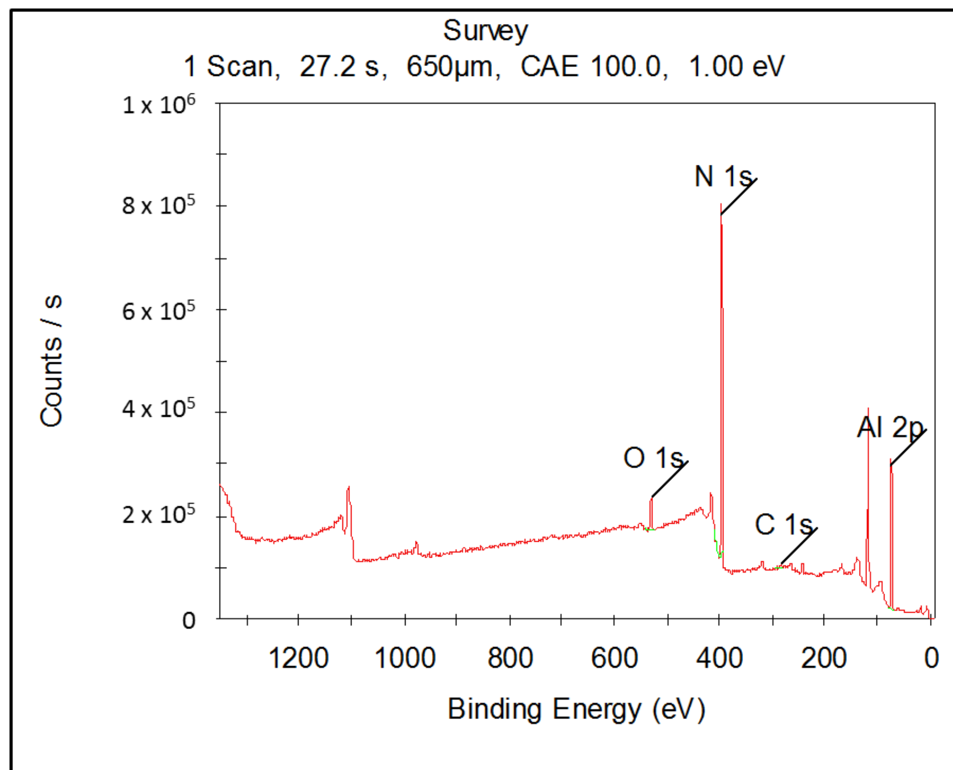

Figure 3-16. Survey spectrum for un-doped AlN thin film

Generally, the basic XPS system consists of four main parts. These parts are the x-ray tube for the generation of x-ray (this part was discussed in XRD section), sample stage manipulator to control the sample position, ultra high vacuum pumping and spectrometer analyzer (photoelectron detector) as shown in figure 3-17.

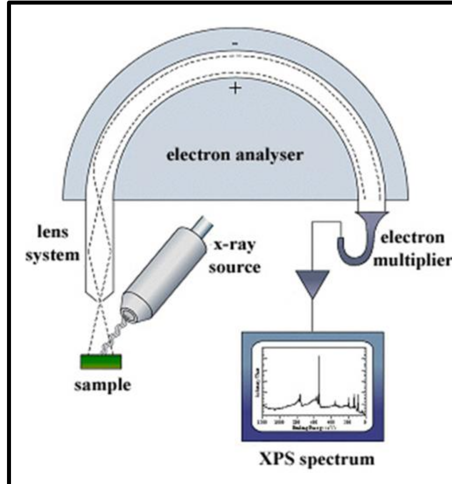

Figure 3-17. Schematics for main XPS components (Tampere University of Technology 2012).

As per Bragg's equation (which was discussed in XRD section), the x-ray source can be monochromated using quartz single crystal to filter the Bremsstrahlung radiation in order to keep only the emission line K_{α} as shown in figure 3-18. The common x-ray sources used in XPS are 1253.6 eV using Mg anode and 1486.6 eV using Al anode. The Monochromator enhances XPS spectra by reducing width of the spectra peaks and the background as illustrated in figure 3-19 [53].

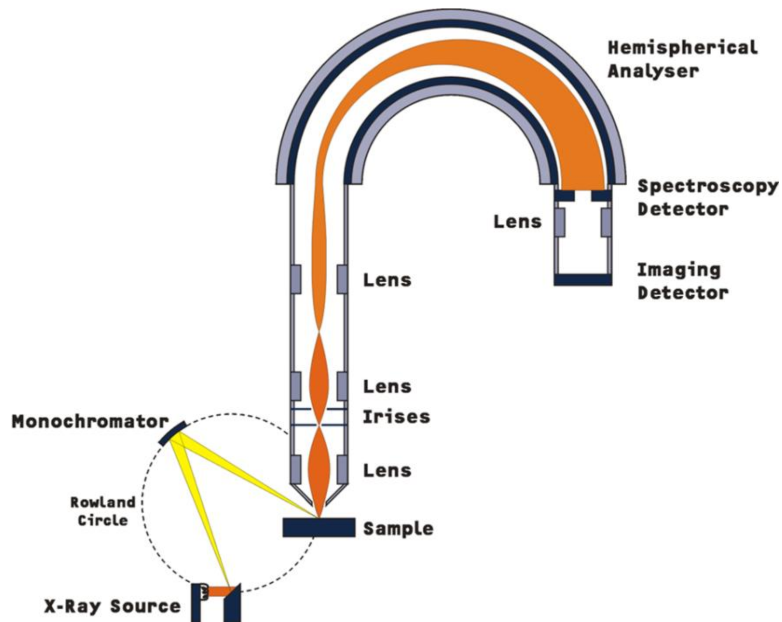

Figure 3-18. X-ray Monochromator in XPS (NanoAnalytics GmbH 2017).

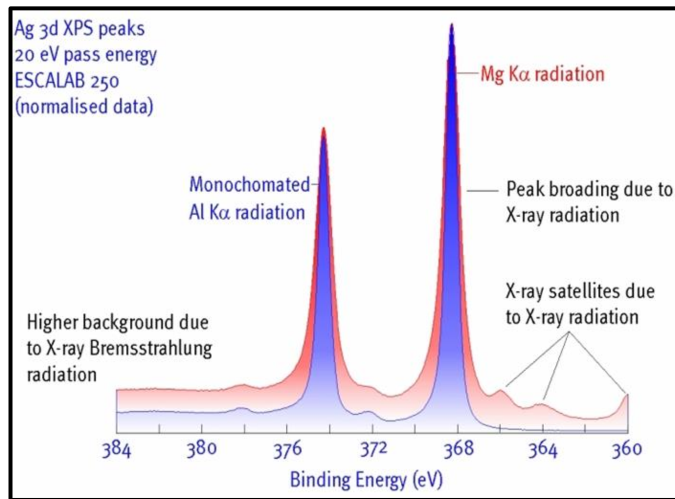

Figure 3-19. XPS spectra with and without Monochromator (Thermo Corporation 2016).

b. Time of Flight – Secondary Ion Mass Spectroscopy (TOF-SIMS)

The TOF-SIMS provides the mass spectroscopy of the existing elements and compounds (atoms and molecules) on the surface, it has high sensitivity suitable for

surface traces analysis. It has the capability of detecting the majority of elements and compounds from ppm to ppb range. It has also a very high mass resolution that can easily give information about the isotopes and its mass range is from 0 to 10000 amu (atomic mass unit) including hydrogen. It is extremely surface sensitive because the analyzed ions are released from the first two atomic layers. To probe through the material depth, TOF-SIMS is usually combined with a sputtering source to enable the depth profiling capability to investigate elements and compounds concentration as a function of depth. This capability is highly required in semiconductor research and development to track the doping and defects as well as secondary phases at the interfaces. Although the TOF-SIMS is highly sensitive, the quantification is quite challenging and requires specialized standard samples.

As per Evans diagram, TOF-SIMS analytical spot size (primary beam sport size) varies from 100 nm to 100 µm and the detection limit which is related to the sensitivity is approximately from 100 ppb to 0.1 %. Its basic principle relies on the bombardment of the material surface by a primary ion beam source of high energy up to 50 keV, these ions collide with the surface of material to generate secondary ions as illustrated in figure 3-20, the primary ions are energetic enough to generate these secondary ions. However, their energy should not exceed certain level to avoid the fragmentation of large molecules [54].

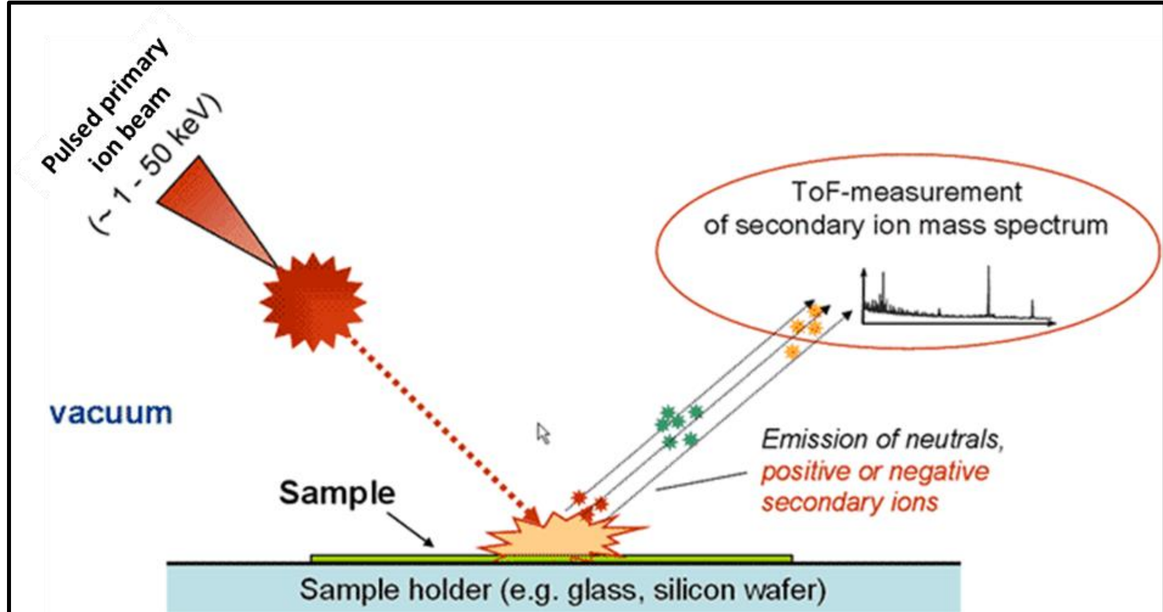

Figure 3-20. TOF-SIMS basic principle.

The secondary ions are extracted and accelerated to the detector by the applied electrical potential difference U as illustrated in figure 3-21 [55]. The simplified physical model relies on the acceleration of the ion of mass m and charge q in electrical potential difference (applied voltage) U and to measure time of flight made through the path S. Equation (3-5) describes the relationship between the mass, charge and the time of light of the ion from the extraction electrode to the detector.

$$t = S \, . \sqrt{\frac{m}{2qU}} \tag{3-5}$$

Where **t** is the time of flight, **S** is the field free drift path, **U** is the applied voltage and **q** is the ion electrical charge.

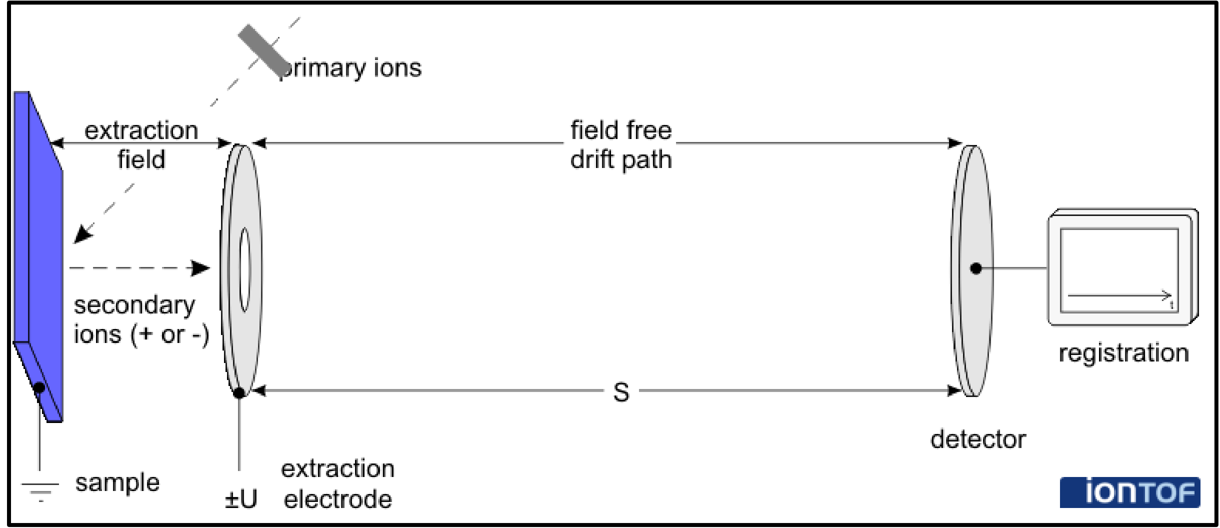

Figure 3-21. Schematic of TOF – mass analysis.

SIMS spectrum provides counts as a function of mass in atomic mass unit (amu). After calibration, the counts are converted to concentration in cm^{-3}. The measurements are performed whether in positive polarity for positive ions or in negative polarity for negative ions as illustrated in figure 3-22 [56].

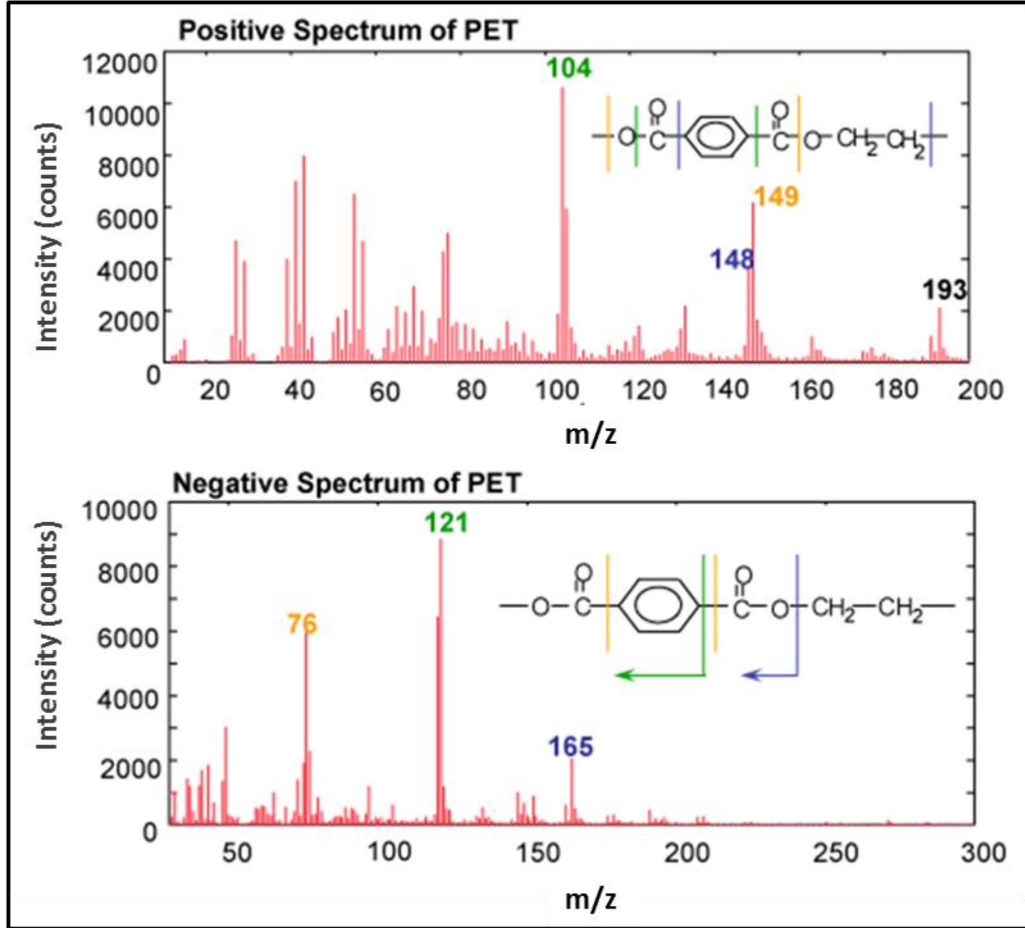

Figure 3-22. TOF-SIMS spectrum for PET sample.

5. Surface Imaging

a. Scanning Electron Microscopy (SEM)

The SEM technique gives a variety of information about the material surface. It provides mainly imaging and surface topography using a focused electron beam which interacts with the surface and generates a magnified image with resolution in the nanometer range. Other information such as the elemental composition and crystal orientation can be obtained when SEM is combined with certain accessories. The spot

size is in the range of few nanometers (sometimes in sub-nanometer range) which provides a high lateral resolution.

As per duality wave-particle concept, the particles such as electrons can be described as waves and particles. Thus electrons behave as waves just like photons (light), however, their associated wavelength is extremely small (approximately 100,000 time shorter than light) as shown in figure 3-23. This very short wavelength of high energy electrons makes them a very good source of “illumination” to “see” very small features.

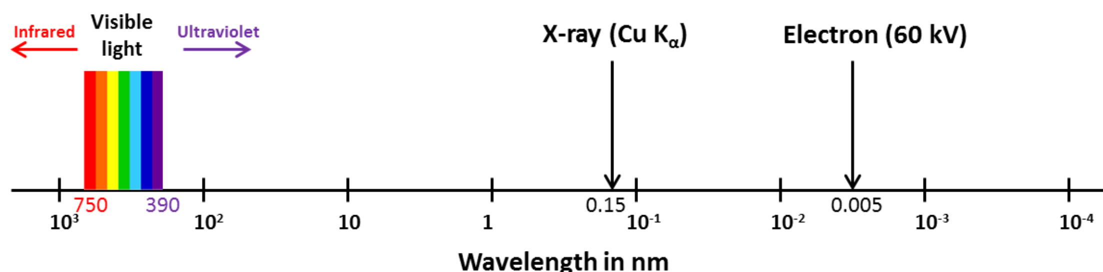

Figure 3-23. Comparison between the wavelength of a 60 kV electron and visible light.

The electron beam is produced at the electron gun and then through the column it is focused and directed toward the sample surface. The electromagnetic lenses and the electronics control the beam focus and raster to scan the selected area as shown in the schematics (figure 3-24) [57].

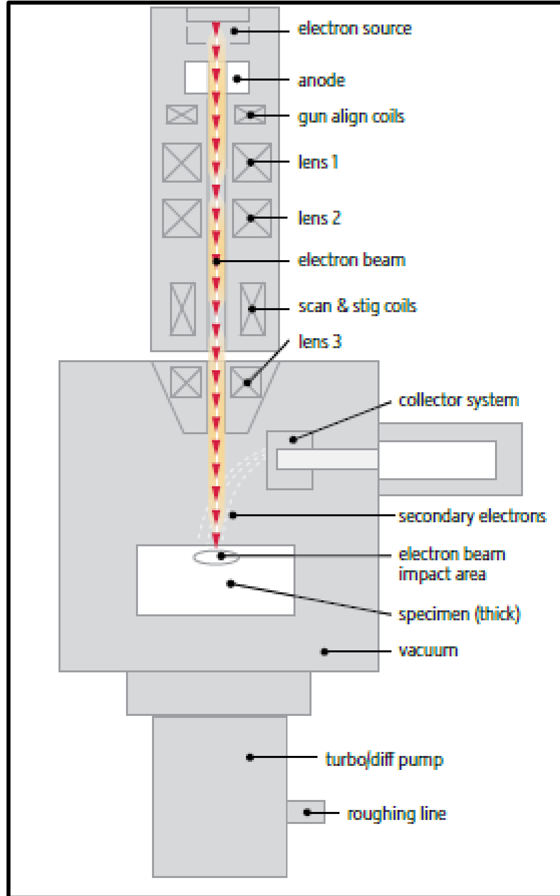

Figure 3-24. Basic components of Scanning Electron Microscope.

The electrons will interact differently with the surface due mainly to chemical composition and morphology. The electron beam interactions with the surface will produce emissions as shown in figure 3-25. Measuring these emissions, namely, secondary electrons provides the imaging capability.

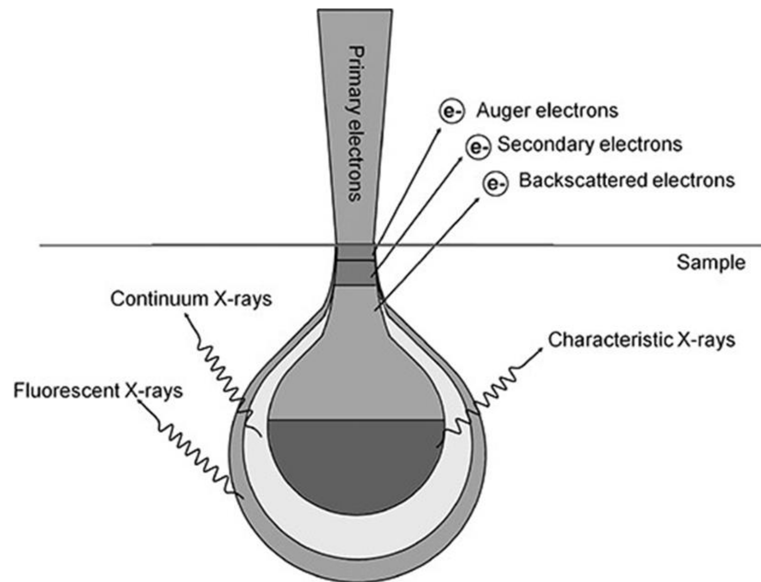

Figure 3-25. Scanning electron microscopy interaction zones and related emissions (Nanotechnologies for the Life Sciences 2007).

b. Atomic Force Microscopy (AFM)

AFM is one of the most multipurpose imaging microscopes at the nanometer scale, it has three main capabilities which are imaging, measuring and manipulating. Firstly, imaging is used to provide three-dimensional images to give idea about the surface morphology. Also the scanning probes collect different localized measured information such as electrical properties, mechanical properties within a small area of the sample surface. Finally, AFM has some manipulation applications such as nanolithography using anodic oxidation by a special tip, this technique can provide a small oxide layers for nanofabrication with high precision.

AFM has very high resolution and can provide imaging with atomic lateral resolution and sub-nanometer height resolution. AFM probe consists on an extremely

sharp tip (less than 10 nm tip radius) on the edge of the cantilever as shown in figure 3-26 [50].

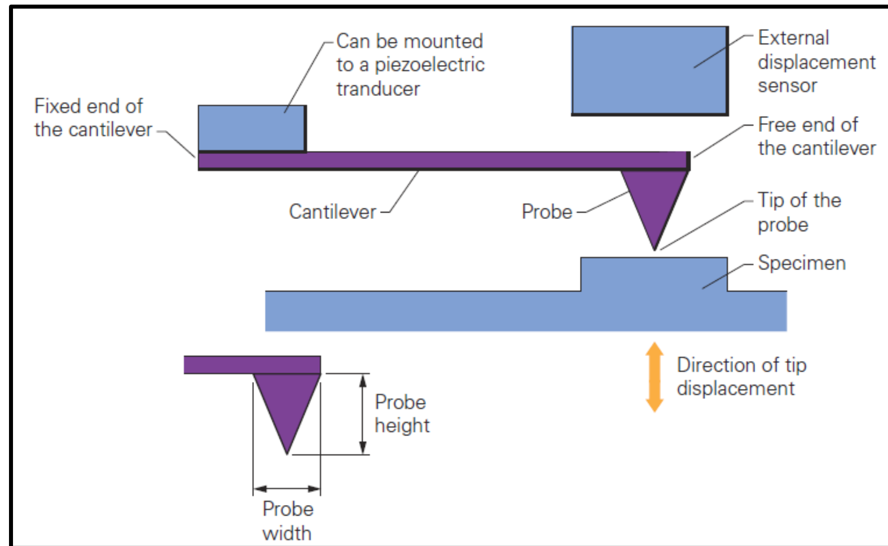

Figure 3-26: AFM cantilever and tip schematic.

AFM basic principle relies on approaching the tip to the sample surface and the interactions with the surface are quantified by sensing the small deflection of the cantilever using a laser source and detector as shown in the figure 3-27 [50]. In the scanning operation, when the probe is deflected, the laser light spot is deviated from the photo-detector center to a (x,y) position. This change in the signal is monitored and processed to provide a three dimensional (3D) image.

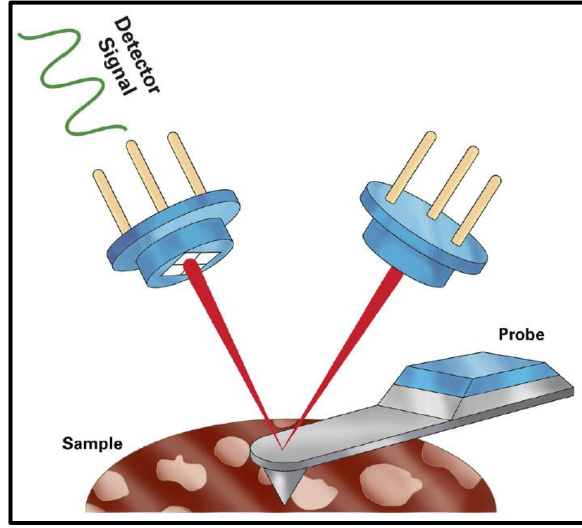

Figure 3-27: Probe deflection sensing schematic.

There are different modes used in AFM, the main modes are Contact Mode and Taping Mode. In Contact Mode, the sharp tip is continuously in contact with the surface and the deflection of the laser spot is directly related to change in height. In Tapping Mode, the probe is in continuous mechanical oscillation and its frequency is close or at its resonance frequency. In this case, the detector measures the cantilever oscillation amplitude and with a feedback mode it adjusts the probe height based on the amplitude signal to maintain the same amplitude set-point. The change in height is measured and processed into a 3D image.

CHAPTER 4: RESULTS AND DISCUSSION

1. MOCVD Growth of Er doped AlN

In this work, Er-doped AlN samples were grown on sapphire substrate using MOCVD system. The precursors were trimethylaluminum (TMA) as Al source and ammonia (NH_3) as N source. Trisisopropylcyclopentadienylerbium was used for the in-situ Er doping. Hydrogen was used as the gas carrier at constant flow of 2 standard liters per minute. Figure 4-1 shows the growth temperature sequence of the Er:AlN epilayer namely heat treatment to remove contaminations from the substrate surface at 1150 °C. Then two AlN buffer layers are deposited, the first buffer layer is 30 nm thick which deposited at 950 °C / 30 mbar and the second buffer layer is 100 nm thick which deposited at 1100 °C / 30 mbar. Then a 1 µm thick AlN template is grown at 1300 °C / 30 mbar, its thickness is 1µm. Finally, an Er-doped AlN layer is grown at 1050 °C / 30 mbar with a targeted thickness of 0.3 µm. The growth temperatures phases for all AlN:Er samples are summarized in figure 4-1. The layer structure of the grown samples un-doped AlN and AlN:Er are shown in figures 4-2 and 4-3.

AlN:Er layer growth is conducted at a much lower growth temperature (1050 °C) compared to the typical growth temperature (1300 °C) for un-doped AlN because Er incorporation will be very low at high temperatures.

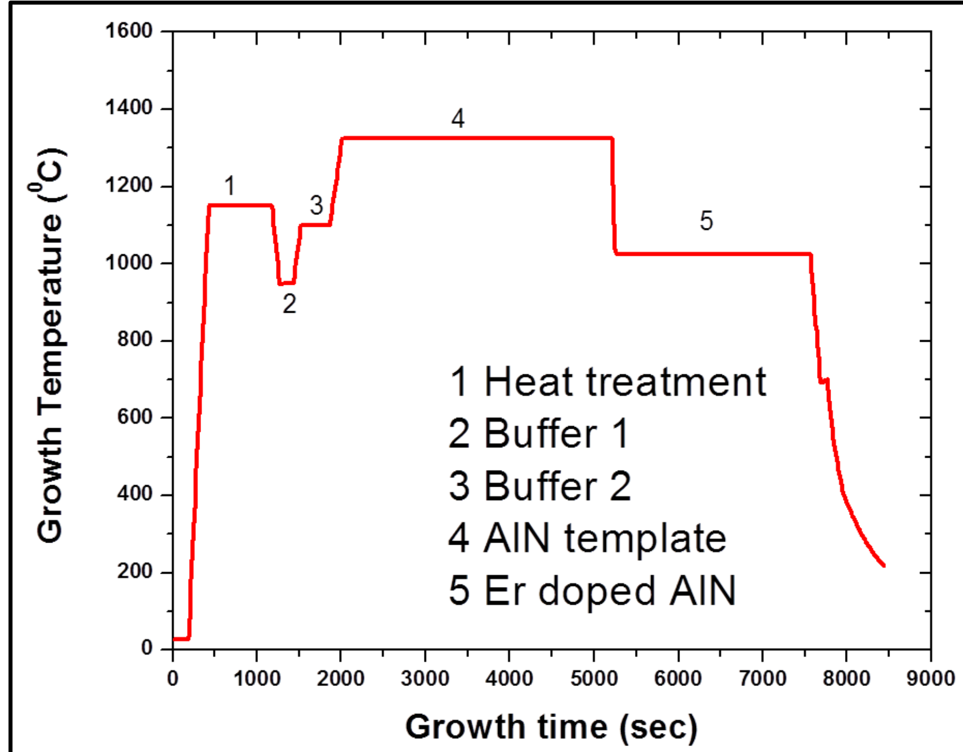

Figure 4-1. Growth temperature sequence of the Er doped AlN epilayer growth on sapphire substrate.

Four samples of Er-doped AlN as shown in figure 4-3 were prepared using the same growth conditions, except, the Er flux which was different for each sample as shown in Table 4-1. The dependence optical and structural properties as well as the surface morphology and chemical composition on the Er molar flux during the growth will be discussed later in this chapter.

The sapphire substrate used for these samples is c-plane oriented single crystal. This crystal orientation is employed in order to grow c-plane AlN thin films.

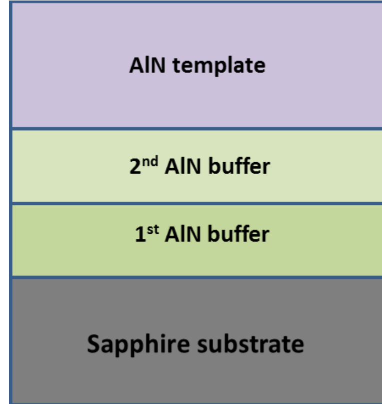

Figure 4-2. Un-doped AlN layers structure.

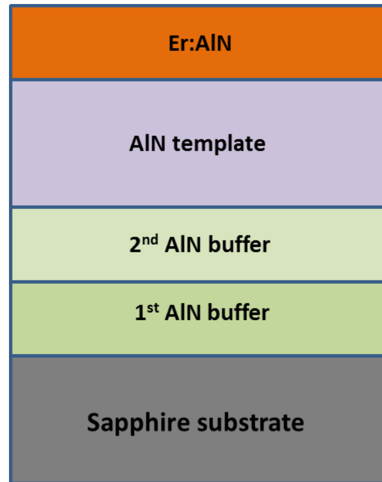

Figure 4-3. AlN:Er layers structure.

Samples	Er flux (µmol/min)	Temperature (°C)
Un-doped AlN	0	1300
Er:AlN (20)	20	1050
Er:AlN (24)	24	1050
Er:AlN (28)	28	1050
Er:AlN (32)	32	1050

Table 4-1. Erbium flux and growth temperature for AlN:Er samples.

2. Structural properties

XRD measurements were performed using PANalytical diffractometer and Bragg-Brentano configuration, the X-ray source is generated in the tube by Copper anode and its K_α characteristic wavelength is 0.154 nm, the scans were performed using 45 kV as high voltage for the tube, 40 mA as current, 0.0131° as step size and 0.263 °/s scan speed. These parameters were used in all samples. The scans in two theta (2θ) were from 20° to 100°. The XRD patterns as well as the rocking curves were used to study the crystalline and structural properties for each sample.

Figures 4-4 to 4-8 show respectively the XRD patterns for un-doped AlN, Er:AlN (20), Er:AlN (24), Er:AlN (28), Er:AlN (32). These samples consist of AlN:Er thin film samples and ine AlN un-doped all grown on c-plane sapphire substrate.

XRD patterns of all samples reveal clearly that the grown AlN thin films exhibit single crystalline structures; only four peaks are present in the XRD patterns. The first peak at 36.05° is related to the diffraction plane (002) of AlN thin film, the second peak at 41.67° is related to the diffraction plane (006) of sapphire substrate, the third peak at 76.44° is related to (004) diffraction plane of AlN and the last peak is at 90.68° is related to (012) diffraction plane of sapphire substrate. The absence of any other peak confirms a single crystalline AlN films.

The XRD patterns demonstrate that AlN thin films have wurtzite c-plane oriented crystal structures. The lattice parameter is calculated from the (002) peak position using

Bragg's equation (4-1):

$$2d_{hkl}\sin\theta = n\lambda \qquad (4\text{-}1)$$

$$d_{hkl} = n\lambda / 2\sin\theta$$

$$\underline{d_{hkl} = 2.488\text{Å} = 0.2488\text{nm}}$$

Where θ is 18.025°, n is 1 and λ is 0.154 nm. Experimentally the inter-planar spacing d_{hkl} of AlN (002) planes is 0.2488 nm. The structure of AlN is hexagonal so the inter-planar spacing is expressed by the equation (4-2):

$$d_{hkl} = \frac{1}{\sqrt{\frac{4}{3}\left(\frac{h^2+hk+k^2}{a^2}\right)+\frac{l^2}{c^2}}} \qquad (4\text{-}2)$$

AlN (002) plane has the parameters h = 0; k = 0; l = 2.

$$d_{hkl} = \frac{c}{l}$$

$$c = d_{hkl} * l$$

$$\underline{c = 4.976\text{Å} = 0.4976\text{nm}}$$

This value of c is very close to the reported value of 0.4982 nm which is matches closely [34].

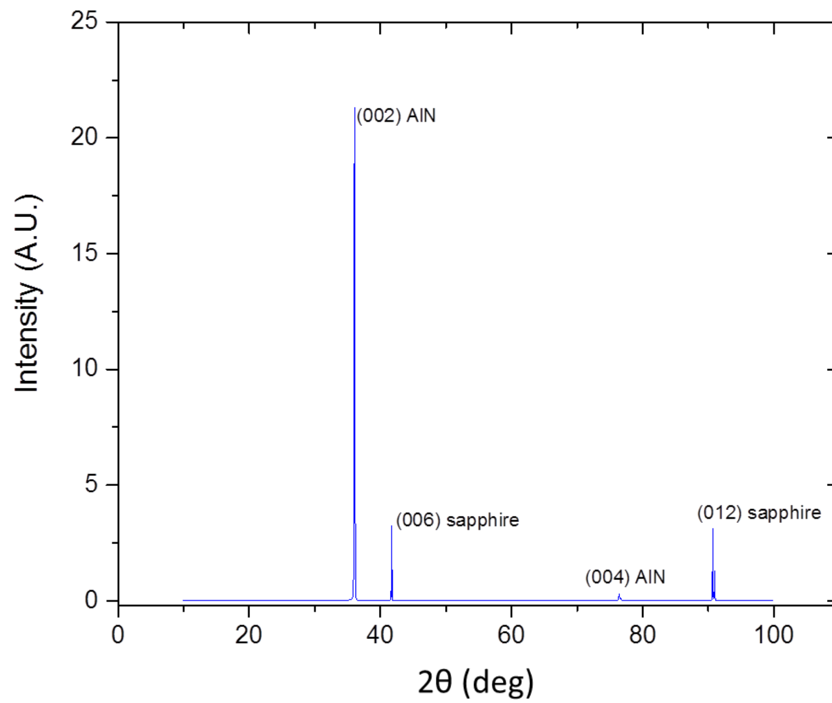

Figure 4-4. XRD theta-2theta scan for un-doped AlN on Sapphire.

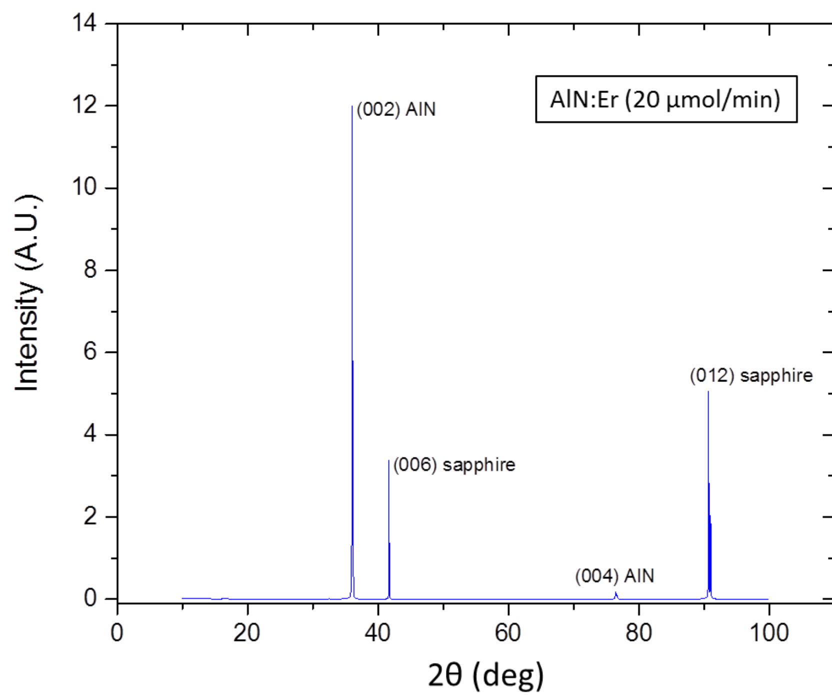

Figure 4-5. XRD theta-2theta scan for AlN:Er (20) sample c-plane AlN on Sapphire.

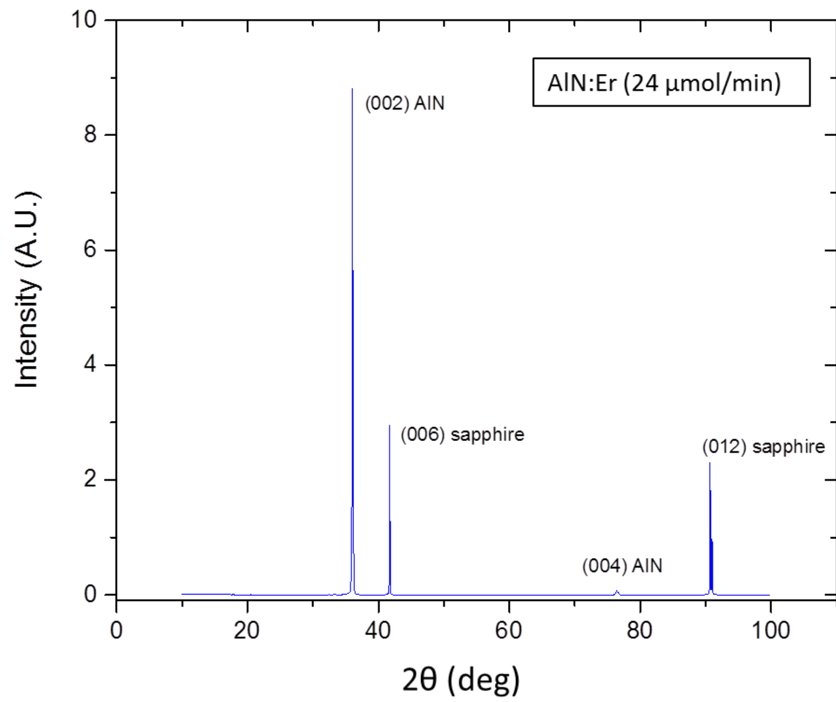

Figure 4-6. XRD theta-2theta scan for AlN:Er (24) sample c-plane AlN on Sapphire.

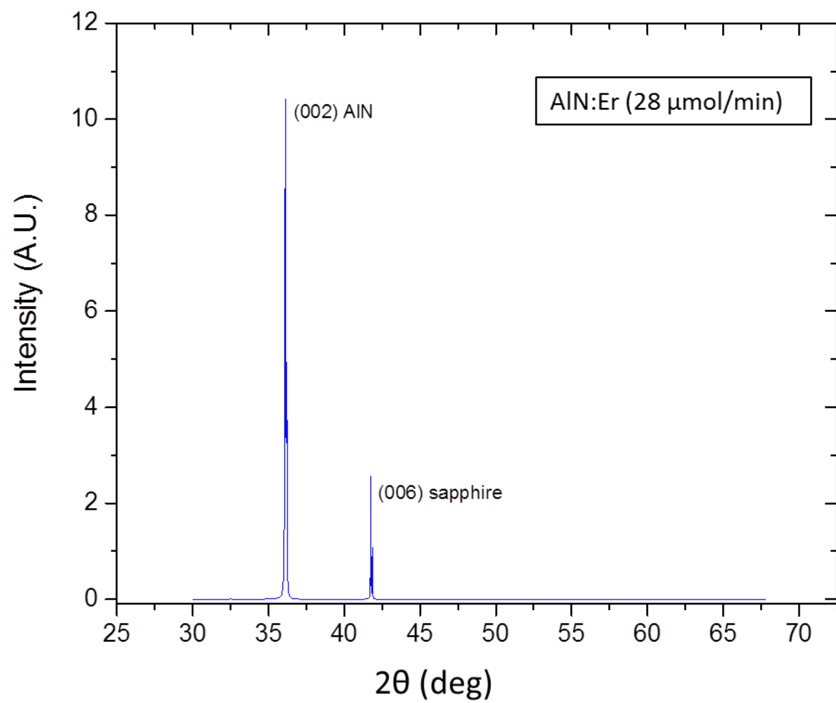

Figure 4-7. XRD theta-2theta scan for AlN:Er (28) sample c-plane AlN on Sapphire.

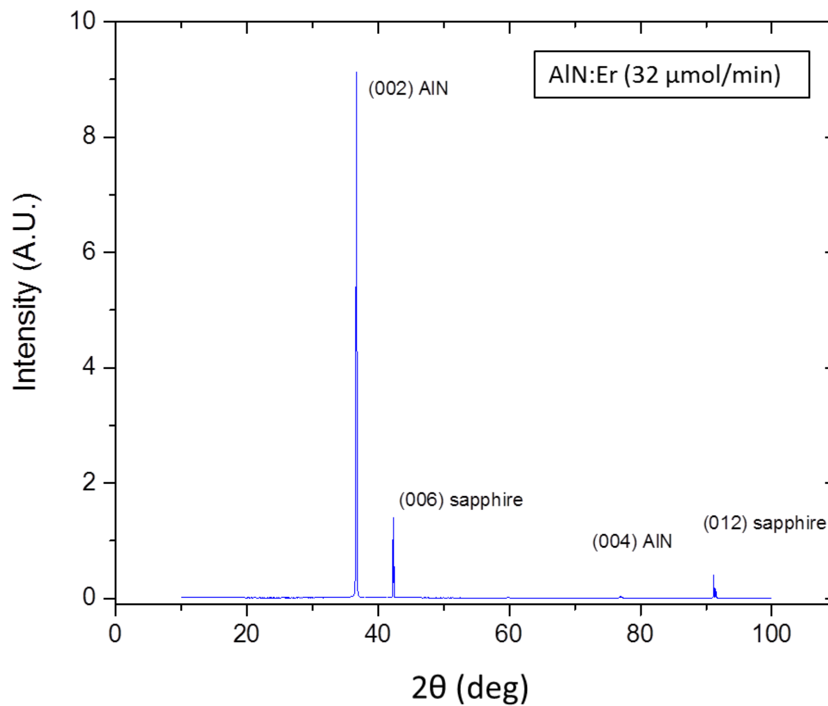

Figure 4-8. XRD theta-2theta scan for AlN:Er (32) sample c-plane AlN on Sapphire.

In order to study the crystalline quality, rocking curve scans are performed at the principal diffraction plane at angle 18.025° by keeping the x-ray tube and the detector at this angle while rocking the sample around this angle, the scans are shown in figures 4-9 to 4-13.

Full Width at Half Maximum (FWHM) which was measured by rocking curve scans are presented in Table 4-2, the value of FWHM is expressed in arcsec unit. The un-doped AlN has a lower FWHM (150 arcsec) which indicate a good crystalline quality. For AlN:Er samples, the crystalline quality is not as good as the un-doped samples mainly because they are grown at much low temperatures to allow for Er incorporation. Increasing FWHM as we increase Er flux could be related to the difference between Er

and Al which creates strain in the material when Er substitutes Al. Figure 4-14 shows rocking curve scans overlay and figure 4-15 shows the FWHM as a function of the Er flux.

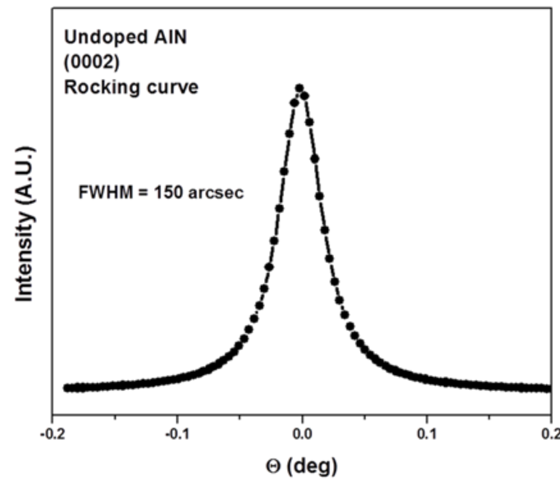

Figure 4-9. Rocking curve measurements for un-doped AlN.

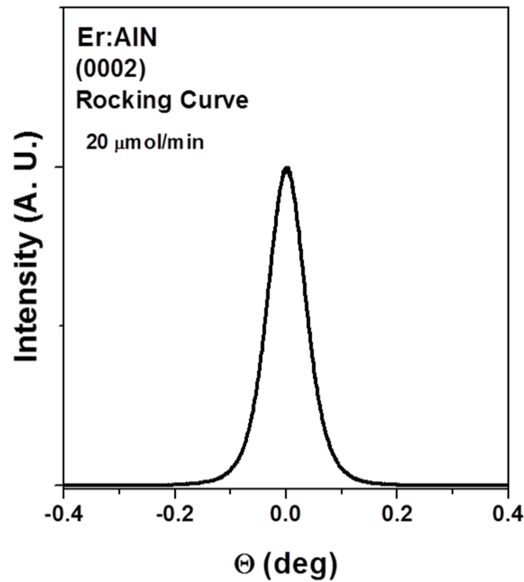

Figure 4-10. Rocking curve measurements for the sample Er:AlN (20).

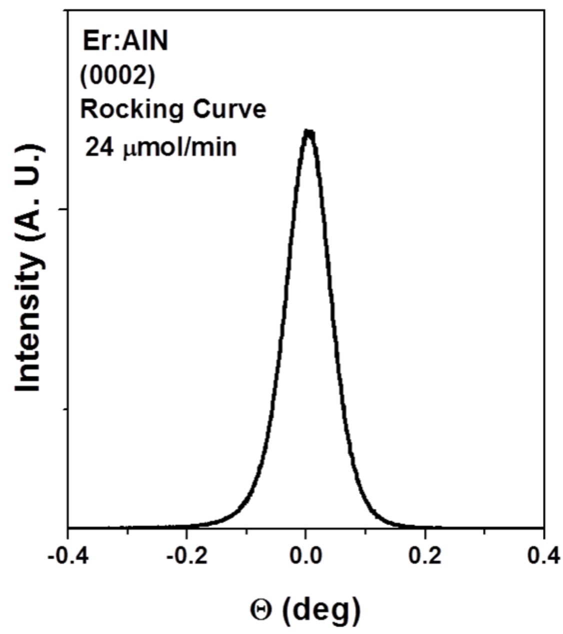

Figure 4-11. Rocking curve measurements for the sample AlN:Er (24).

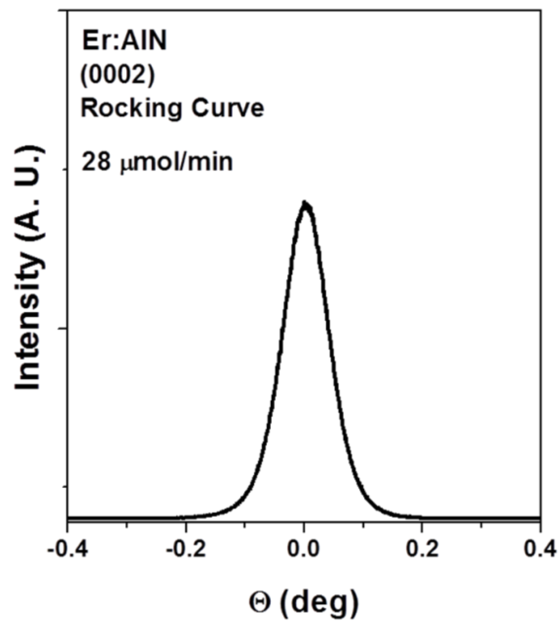

Figure 4-12. Rocking curve measurements for the sample AlN:Er (28).

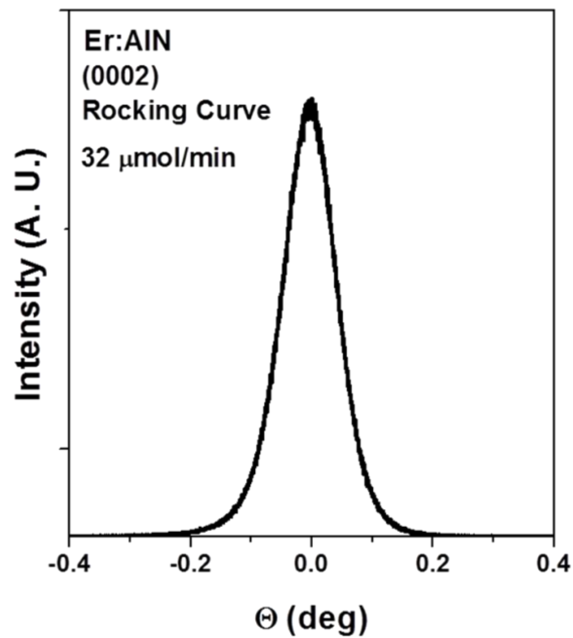

Figure 4-13. Rocking curve measurements for the sample AlN:Er (32).

Table 4-2. FWHM of AlN:Er samples.

Er flux (μmol/min)	**AlN (002) FWHM (arcsec)**
Un-doped AlN	150
20	300
24	334
28	347
32	390

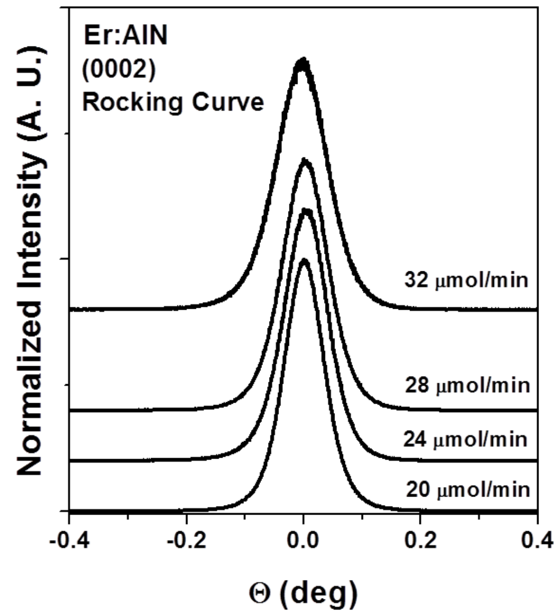

Figure 4-14. Rocking curve measurements overlaid for all AlN:Er samples.

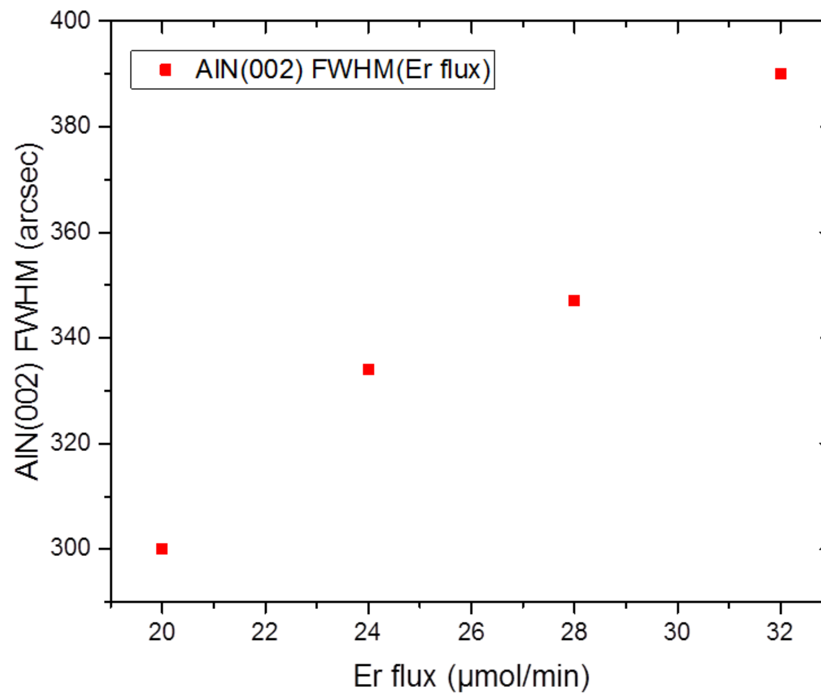

Figure 4-15: FWHM of (002) rocking curve of Er:AlN as a function Erbium flux.

3. Surface analysis (chemical composition)

a. X-ray Photoelectron Spectroscopy

In order to reveal the chemical composition at the surface, XPS measurements were performed by Thermo Scientific Escalab 250Xi spectrometer, the X-ray source a monochromated Aluminium anode (Al K-alpha 1486.6 eV), the spectrometer is equipped with MAGCIS (Monatomic And Gas Cluster Ion Source) Argon ion sputtering source for cleaning and etching, the system has also the flood electron source for charge compensation. The spectrometer is regularly calibrated using three standards Gold, Silver and Copper. The XPS software is Avantage and it has both capabilities spectrometer operations and data analysis. Performing the XPS analysis was part of this thesis.

Aluminium Nitride is a wide bandgap semiconductor and it behaves similar to insulators in XPS scans. When the generated photoelectrons leave the surface, the latter loses the electrical neutrality due to positive charge accumulation. This accumulated charge acts as an electrical potential and shift the photoelectrons energy, this shift is clearly observed on the XPS spectra of insulators without charge compensation. For this, Charge compensation was employed and Carbon 1s peak at 284.8 eV is used as reference for all measurements to correct the charge shift.

In literature, there are many reports about binding energies (BE) of AlN and Al_2O_3, Table 4-3 summarizes several different binding energies for metallic Al, Al-N and Al-O. AlN state aluminium (Al-N) Al2p BE varies from 73.1 to 74.6 eV while Al_2O_3 state aluminium (Al-O) Al2p BE varies between 74.0 and 75.5 eV. It was reported that

Al-N-O binding energy is 75.4 eV which is quite similar to Al-O state aluminium in terms of binding energy [58].

Table 4-3. Metallic Al, Al-N state Al and Al-O state Al binding energies.

Binding energy (eV)				
Al⁰	*Al-N*	*Al-O*	*ΔE (eV)*	References
72.8	74.1 74.3	74.7 75.2	0.6 0.9	(Stanca, 2004)
	74.6	75.4 (*spinel*)	0.8	(Sohal et al., 2006)
72.8	74.1 73.6	74.7 74.6	0.7 1.0	(Jose et al., 2010)
72.8	74.4	75.2	0.8	(Wang et al., 1997)
72.7 72.8 72.5	74.5 74.6	75.5 75.6	1.0 1.0	(Gredelj et al., 2001)
	73.1	75.1 74.2 (*spinel*)	2.0 1.1	(Richthofen et al., 1996)

The XPS measurements were performed after 120s of high energy etching (3KeV) using monoatomic Argon ions. Survey spectra were performed to have a preliminary indication about the present elements on the surface as shown in figure 4-16 and narrow scans with higher resolution were performed for Aluminium *Al2p*, Nitrogen *N1s*, Carbon *C1s* and Oxygen *O1s* as shown in figures 4-17 to 4-20. In this section only un-doped AlN will be presented. Er cannot be detected as XPS is not suitable for doping element measurements in ppm and ppb range, the detection limit of XPS is generally around 0.1%.

Survey spectrum shows the elemental presence of Aluminium, Nitrogen, Oxygen, Carbon and Argon. Carbon presence due to the adventitious hydrocarbon contamination present in the atmosphere, Oxygen indicates the oxidation of AlN surface due to presence

of Oxygen in air. Argon was implanted during the cleaning using Argon ion etching source. The quantitative measurements were performed using narrow scans, beam width was 650µm, Pass-energy was 20.00eV using ALTHERMO1 database for Atomic Sensitivity Factors. Table 4-4 summarizes the atomic concentration of each element. Argon concentration was removed as it was not originally in the samples.

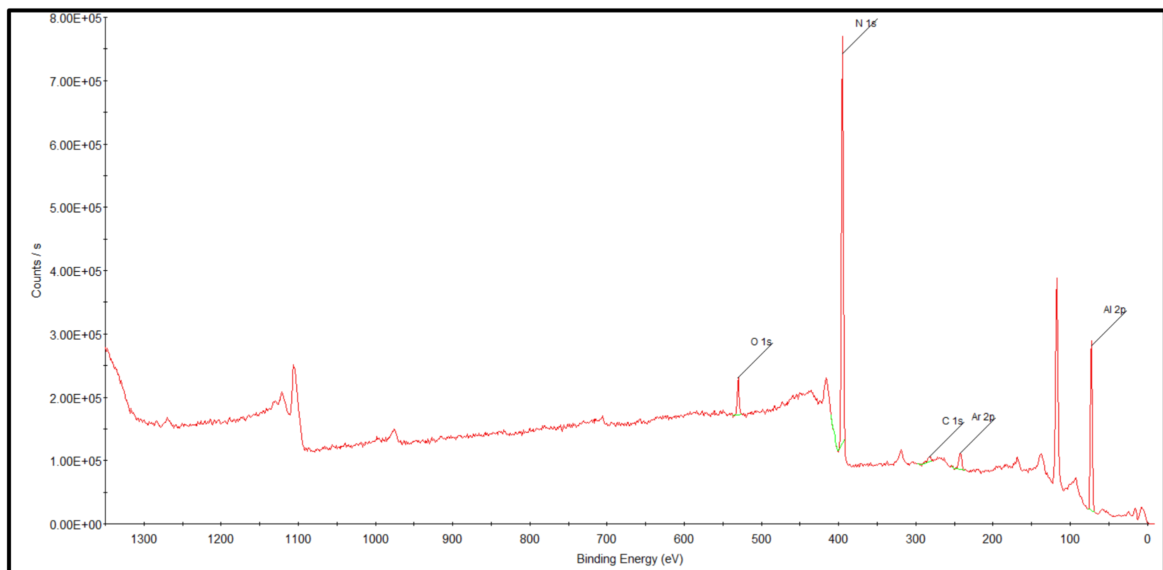

Figure 4-16. XPS Survey spectrum for un-doped AlN.

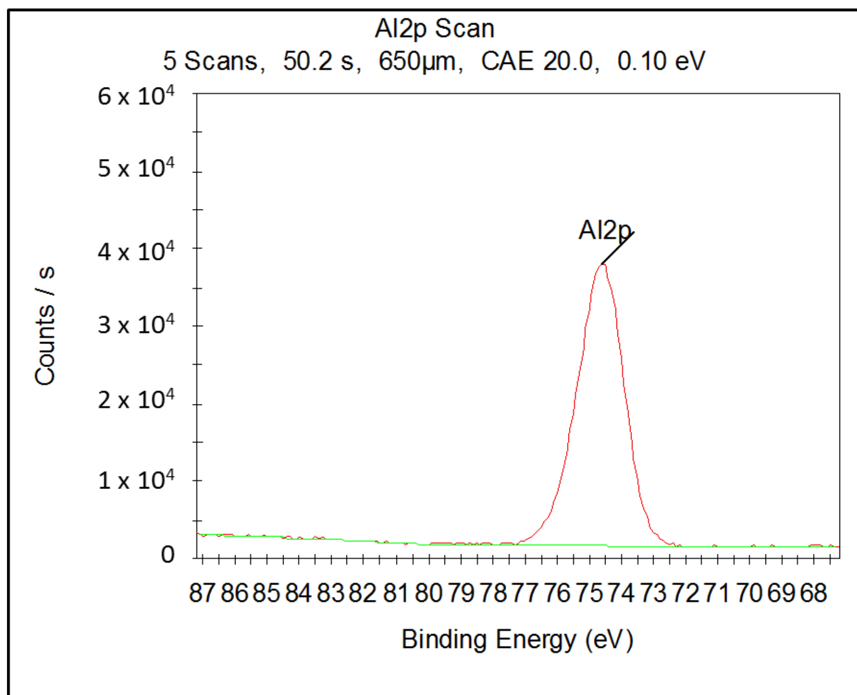

Figure 4-17. XPS Al2p narrow scan for Er:AlN (32).

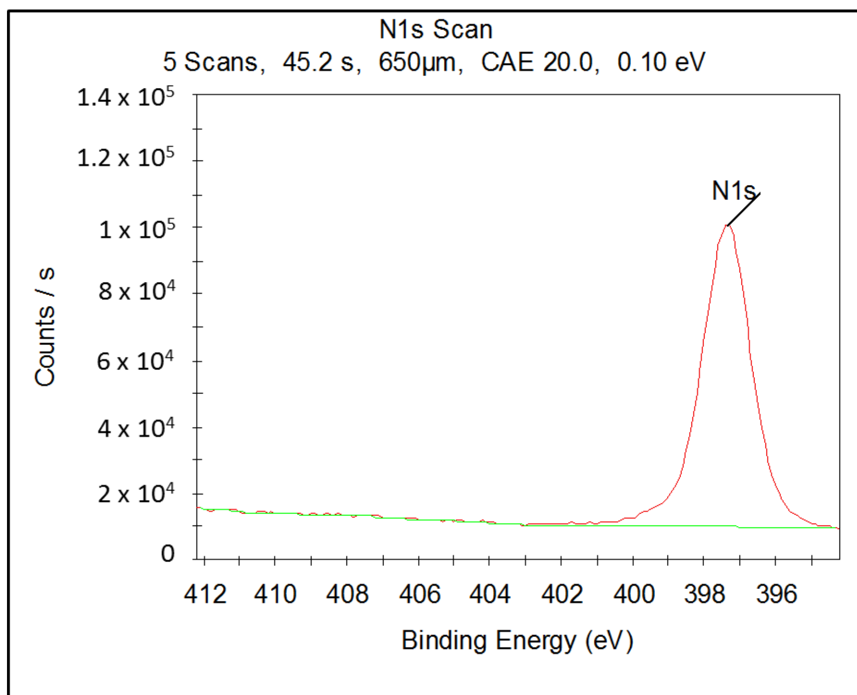

Figure 4-18. XPS N1s narrow scan for Er:AlN (32).

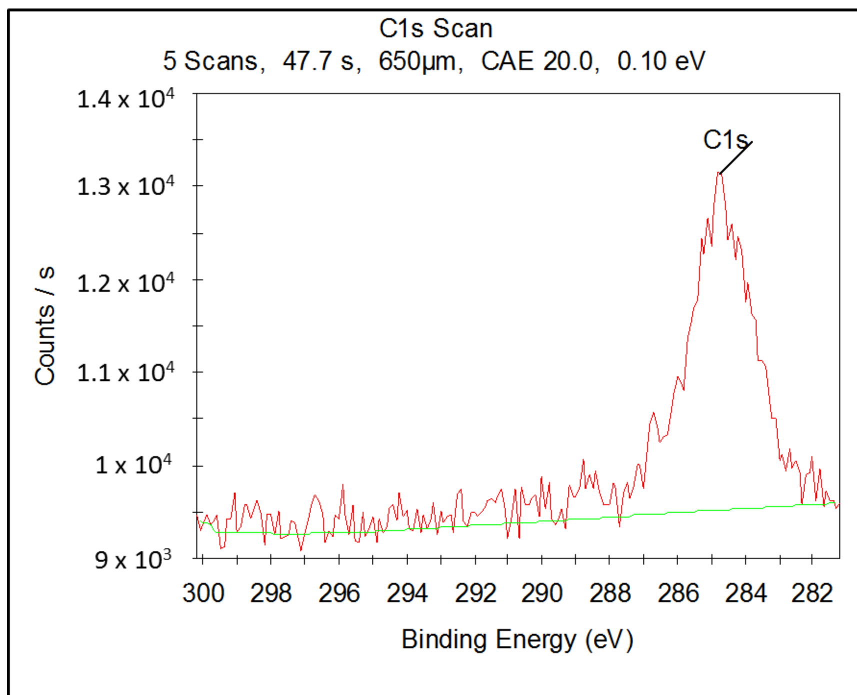

Figure 4-19. XPS C1s narrow scan for Er:AlN (32).

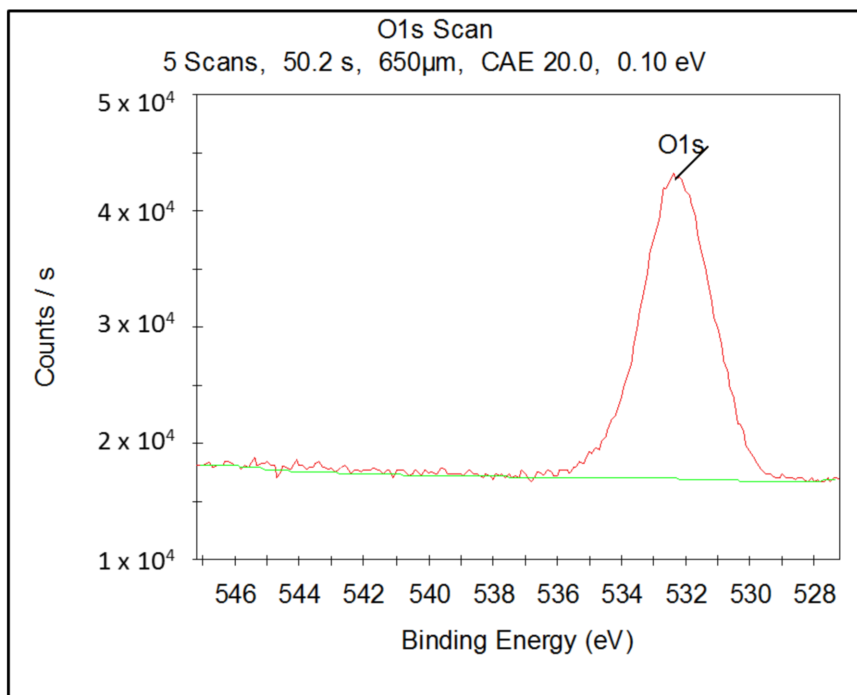

Figure 4-20. XPS O1s narrow scan for Er:AlN (32).

Table 4-4. Surface atomic concentration for Er:AlN (32) using narrow scans.

Name	Peak BE (eV)	FWHM (eV)	Area (P) CPS.eV	Atomic (%)	SF
Al2p	74.6	1.63	64598.06	45.04	0.56
N1s	397.36	1.53	159175.5	39.75	1.676
O1s	532.29	2.48	72766.25	11	2.881
C1s	284.73	2.08	10329.31	4.21	1

The Al2p peak was clearly asymmetric which reveals the presence of a smaller secondary peak with higher binding energy; the suggested fitting was in accordance with the literature such as in I. Scanta report [59]. The energy difference ΔE(eV) between Al2p (Al-N) and Al2p (Al-O) is 0.9eV which is aligned with the previous reports shown in Table 4-3. These results are close to previous results in literature for AlN and Al_2O_3 [58-60]. Figure 4-21 shows the fitting for Al2p identifying the two chemical states Al-N and Al-O and Table 4-5 shows the elemental composition including Al chemical states.

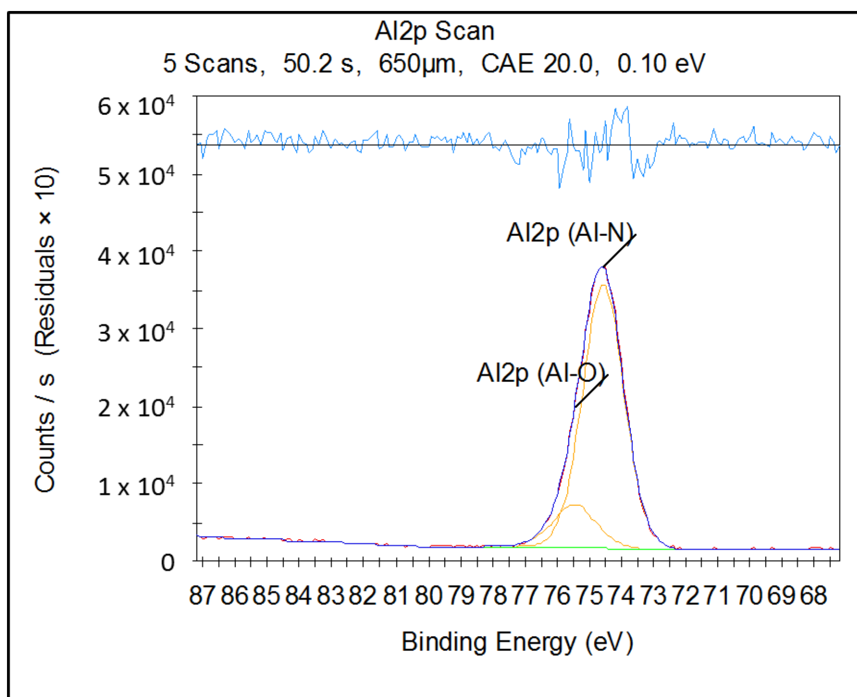

Figure 4-21. Narrow scan Al2p spectrum fitting for Er:AlN (32).

Table 4-5. Surface atomic concentration for un-doped AlN using narrow scans including Al chemical states.

Name	Peak BE (eV)	FWHM (eV)	Area (P) CPS.eV	Atomic (%)	SF
N1s	397.36	1.53	159175.5	39.83	1.676
Al2p (Al-N)	74.55	1.49	54919.78	38.36	0.56
O1s	532.29	2.48	72766.25	11.02	2.881
Al2p (Al-O)	75.45	1.55	9414.49	6.58	0.56
C1s	284.73	2.08	10329.31	4.21	1

b. Time of Flight - Secondary Ion Mass Spectrometer

TOF-SIMS is a powerful technique for sensing the doping elements and compounds in the ppm and ppb range. The system used for all samples is IonTOF TOF.SIMS 5 – 100, Bismuth primary source used at 30kV voltage, it provided 28nA ion current and the analyzed area is crater of 102x102μm^2. The O_2 source was used as sputtering source used at 2kV voltage; it provided 610nA ion current and sputtered a crater of 300x300μm^2 as shown in figure 4-22 before sputtering and 4-23 after sputtering. The analyzer was set in positive polarity for positive ion detection and charge compensation was activated to neutralize the charges accumulated at AlN surface. Performing the TOF-SIMS analysis was part of this thesis. In this study the elemental distribution was investigated throughout the depth using O_2 source for the positive ions Al^+, C^+, H^+, Er^+, N^+. O^+ ion was not explored as O_2 sputtering source was used for sputtering and its intensity will not be significant as it represents the oxygen ions that were present originally in the sample as well as the ones implanted during the sputtering. Direct measurements of doped layer thickness requires the calibration of the etching rate

which was performed by measuring the depth of the etched crater using optical profiler (confirmed by stylus profiler Dektak) to correlate the sputtering time to depth. In two craters, the etching rate was 0.750 nm/s and 0.754 nm/s (average is 0.752 nm/s) using 2 kV and 610 nA sputtering source for AlN:Er samples. These results allow us to convert the SIMS profiles from sputtering time to depth which are shown in figures 4-24 and 4-25.

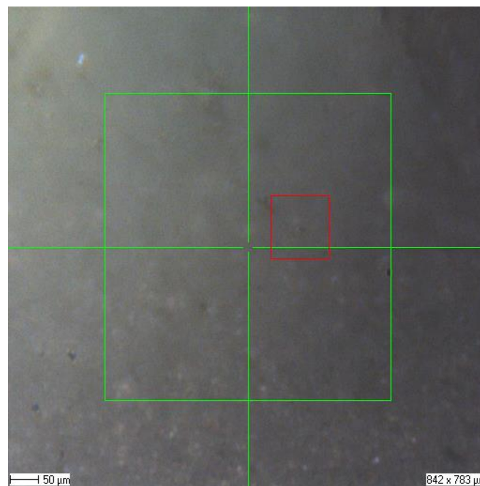

Figure 4-22. Er:AlN (32) surface before sputtering.

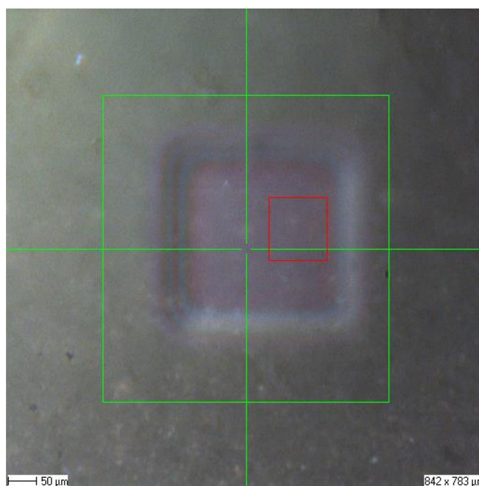

Figure 4-23. Er:AlN (32) surface after sputtering.

The TOF-SIMS sensitivity is different for each element and configuration. Positive ions have higher sensitivity in positive polarity mode such as Al^+, Er^+ and H^+ and O_2 sputtering source in this analysis is recommended for positive ions. The quantification of TOF-SIMS profiles is highly challenging and requires specialized standards for concentrations measurements. In this study, the main objective is to evaluate the Erbium ion intensity for samples AlN:Er (28) and AlN:Er (32) and investigate the elemental distribution as a function of depth especially for Erbium in the AlN:Er layer.

Figure 4-25 shows the distribution of Er^+ in the AlN doped layer as a function of depth for two samples AlN:Er (28) and AlN:Er (32). The profiles show that the intensity of AlN:Er (32) is higher than AlN:Er (28) which reveals that the concentration of Erbium in AlN:Er (32) is higher than AlN:Er (28). The profiles also confirm that the Er is uniformly distributed in both samples throughout the doped layers. It can be seen from

the same figure that the doped layer thickness is close to 300 nm for both samples which matches the target thickness.

Figures 4-26 and 4-27 are TOF-SIMS profiles for AlN:Er (28) and AlN:Er (32). They show that the Er, Al, N intensities have initially low value while carbon and hydrogen have higher values. Then Al, Er and N intensities get higher in the first few seconds of etching until reaching a maximum value; then the intensities decreases slightly until reaching a stable and steady value throughout the etching process. These TOF-SIMS profiles show the intensities in log scale and confirm that Aluminium and Nitrogen are uniformly distributed and also Er is uniformly distributed throughout the doped layer until certain depth where the intensity decreases to a lower value, this can be explained as the etching reached the template layer which is the underneath layer. There was a slight increase of Al intensity while Er was decreasing, it is suggested that Er was preferentially occupying Al lattice. Carbon and hydrogen intensities have relatively high intensities in the first nanometers; this indicates the hydrocarbon contamination on the samples surface. These measurements were performed in positive polarity.

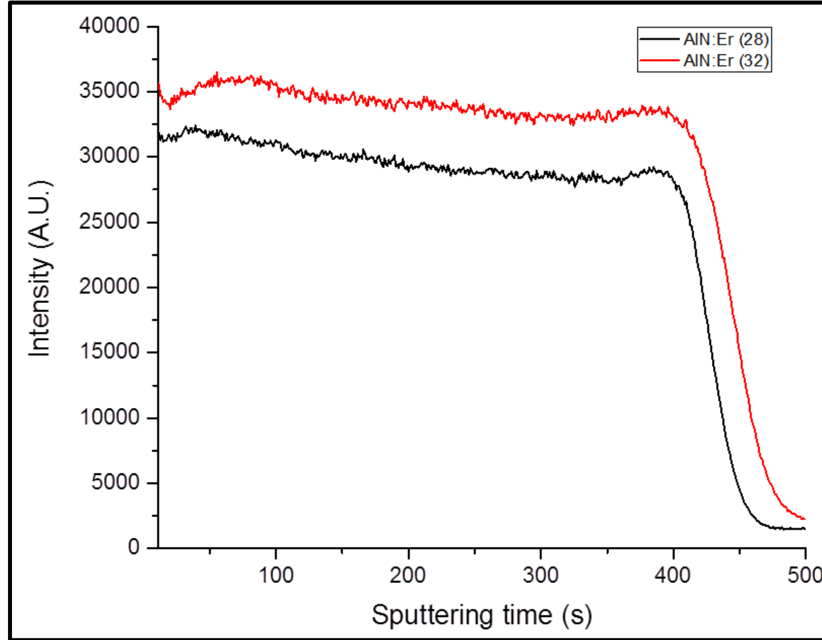

Figure 4-24. Er^+ TOF-SIMS profiles for Er:AlN (28) and Er:AlN (32) in linear scale as a function of sputtering time.

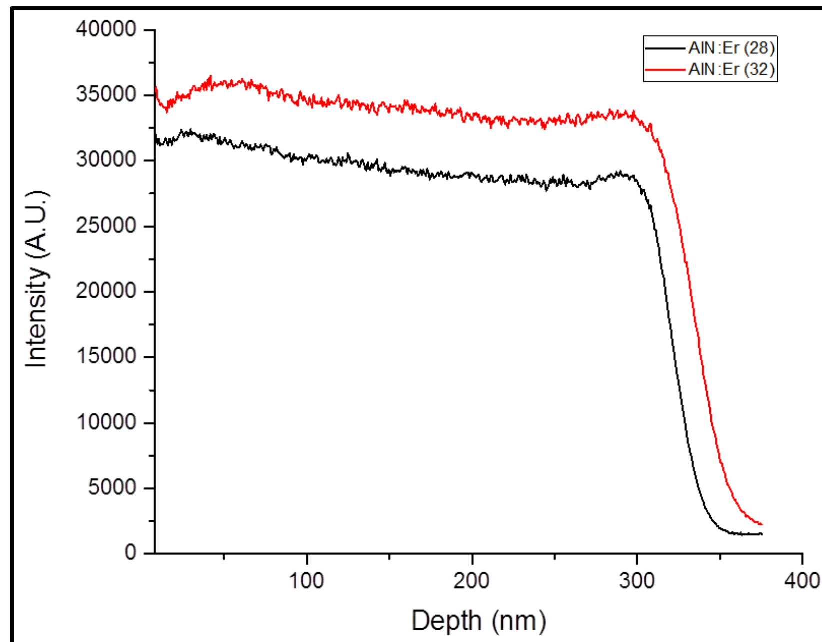

Figure 4-25. Er^+ TOF-SIMS profiles for Er:AlN (28) and Er:AlN (32) in linear scale as a function of depth.

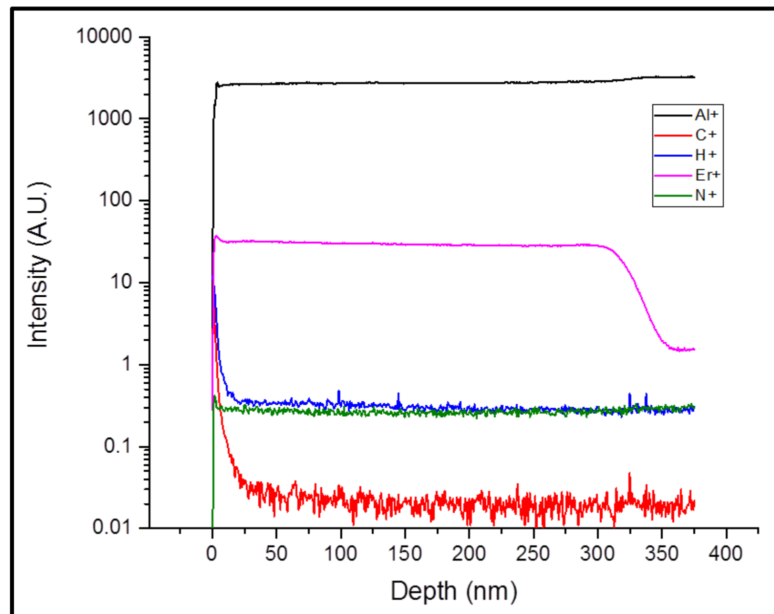

Figure 4-26. TOF-SIMS profiles for Er:AlN (28) in log scale as a function of depth.

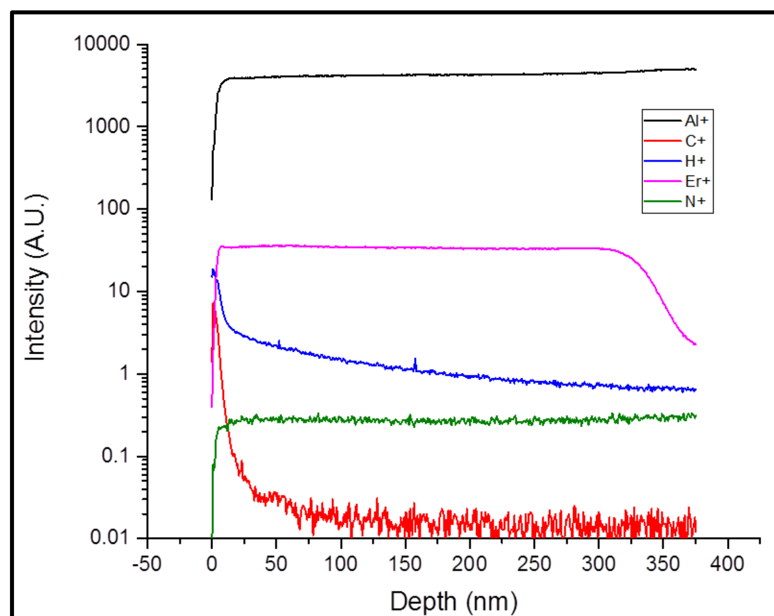

Figure 4-27. TOF-SIMS profiles for Er:AlN (32) in log scale as a function of depth.

TOF-SIMS results shows that Er concentration in the doped AlN layer increases when the Er flux increase as expected. The Erbium atoms are uniformly distributed over

the doped AlN layer and the thickness of the doped layer is around 300 nm which is matching the target thickness.

4. Surface morphology

a. Scanning Electron Microscopy.

The SEM system was used to investigate the surface morphology in the nano-scale for Er:AlN samples. AlN material is a wide bandgap semiconductor and behaves in SEM similar to an insulator. While scanning by the electron beam, the accumulated charges on the surface affect the image quality and resolution. This problem can be resolved by using sophisticated SEM tools equipped with the low vacuum capability which reduces greatly the charging effect by introducing very low concentration of moisture to evacuate the charges.

FEI Quanta 250 SEM was used for all samples the AlN:Er (figures 4-28 to 4-31) to study the surface morphology. The surface exhibits a non-uniformity for all samples. Figures 4-28 and 4-29 represent AlN:Er (20) and AlN:Er (24) and show the presence of clear sharp edges and some of interconnected island-like features. Figures 4-30 and 4-31 represent SEM image for AlN:Er (28) and AlN:Er (32) show that the surface is characterized by sharp edge island-like features which are randomly distributed in the nano-scale. These results suggest that the island-like features concentration has been increased while increasing the Er flux.

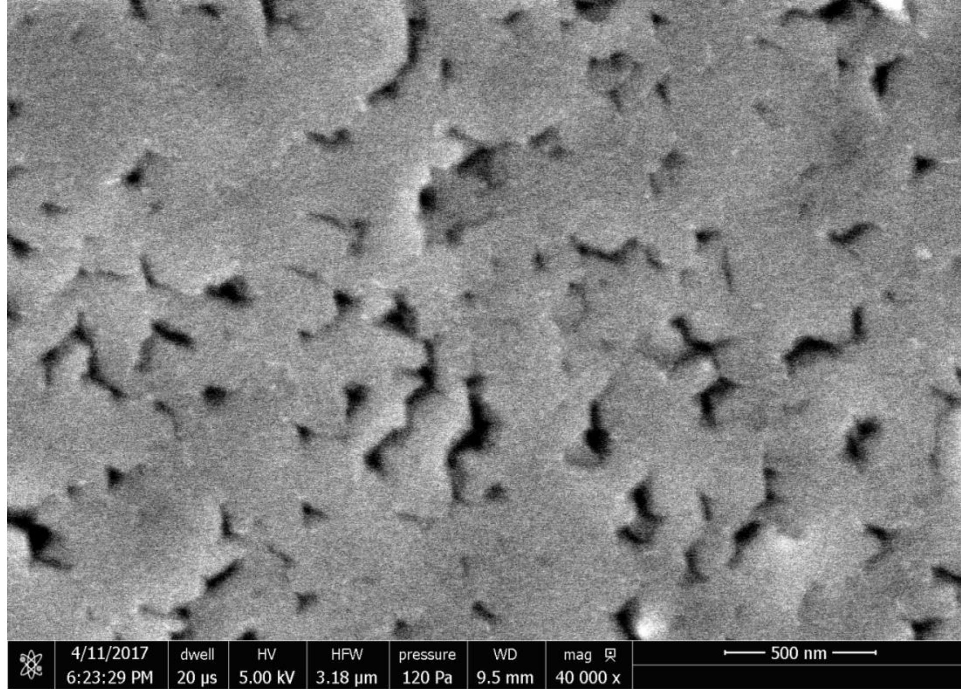

Figure 4-28. SEM image for AlN:Er (20).

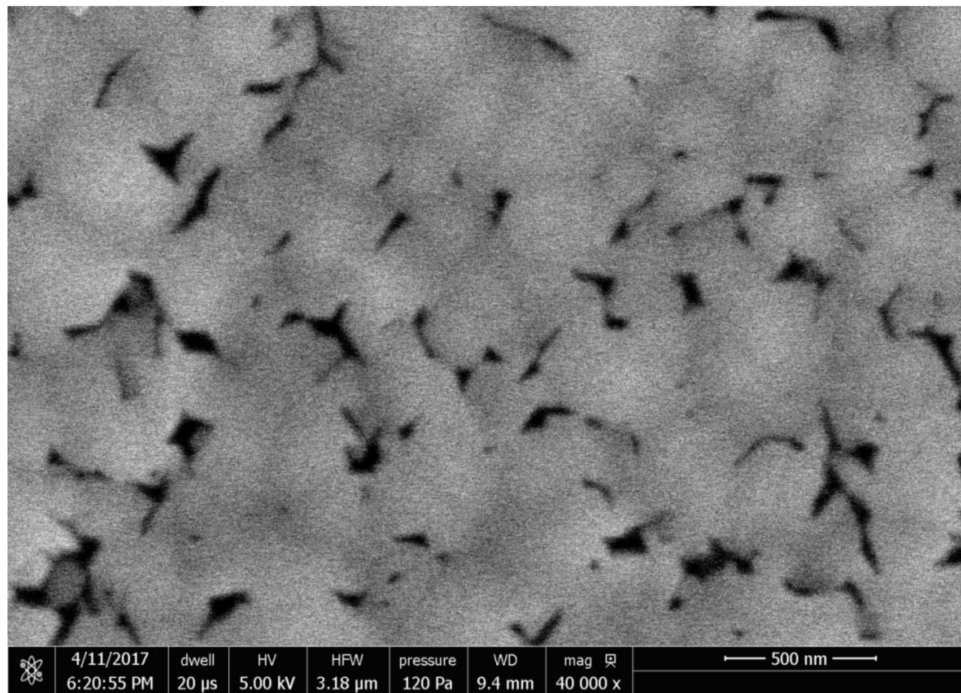

Figure 4-29. SEM image for AlN:Er (24).

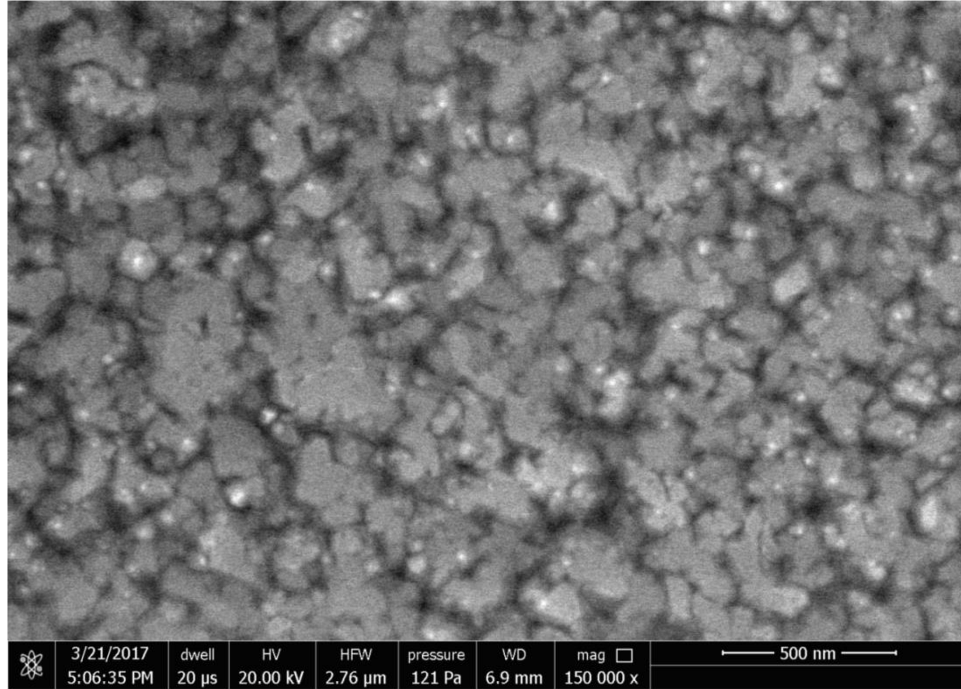

Figure 4-30. SEM image for AlN:Er (28).

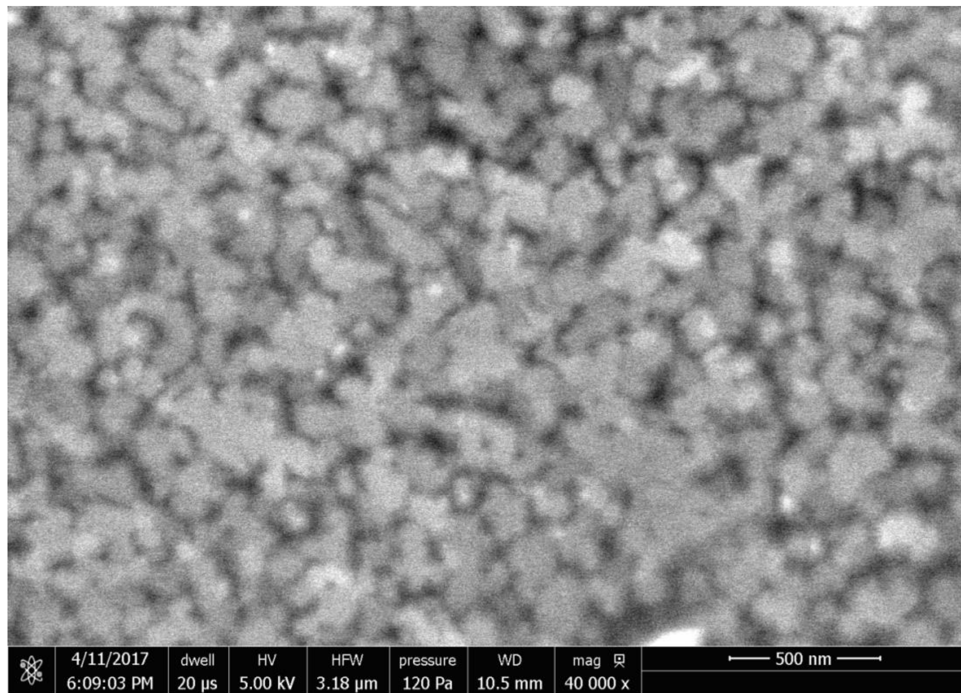

Figure 4-31. SEM image for AlN:Er (32).

b. Atomic Force Microscopy

AFM is a surface analysis technique which gives an idea about surface morphology along with other properties using different accessories. Bruker Icon AFM using tapping mode was employed in this investigation as a complementary technique for SEM, surface morphology was identified and the surface roughness was measured. Performing the AFM scans was part of this thesis. Roughness analysis was based on root mean squared parameter known as R_q or RMS on selected area of $1x1\mu m^2$. More details are available in the appendix. Figure 4-32 is the AFM image of AlN:Er (20), it shows sharp edges at the surface similar to the SEM image and provided roughness measurements of 2.69 nm. Figure 4-33 is for AlN:Er (24), it exhibits the presence of interconnected island-like features and the roughness is 4.29 nm. Figure 4-34 is for AlN:Er (28) shows that concentration of island-like features is higher than AlN:Er (24) and the roughness is 5.80 nm. Figure 4-35 is for AlN:Er (32) and shows that the island-like feature concentration is higher than AlN:Er (28) and the roughness is 6.30nm. The roughness measurements are summarized in Table 4-6.

Table 4-6. Surface roughness measurements for AlN:Er samples.

Er flux (μmol/min)	Surface roughness (nm)
20	2.69
24	4.29
28	5.80
32	6.30

It is clear that the island-like concentration increases linearly with Erbium flux; however, there is clear increase of surface roughness with increase of Er flux.

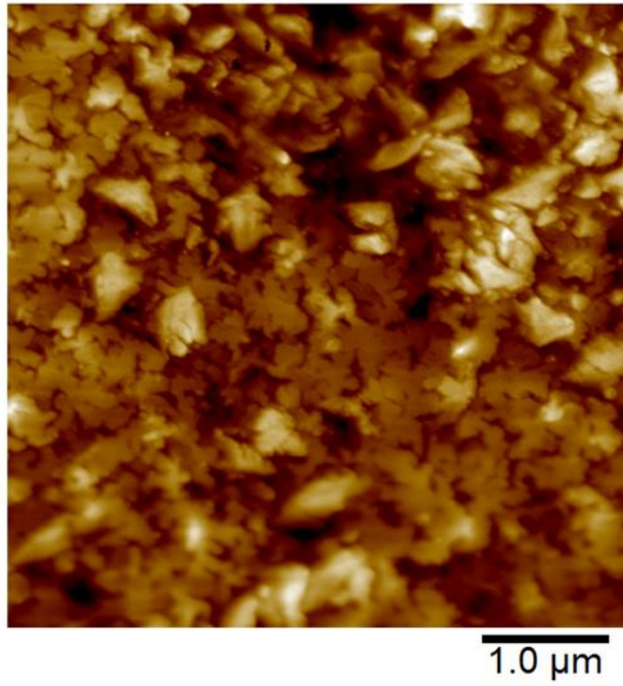

Figure 4-32. 5x5um2 AFM image for AlN:Er (20).

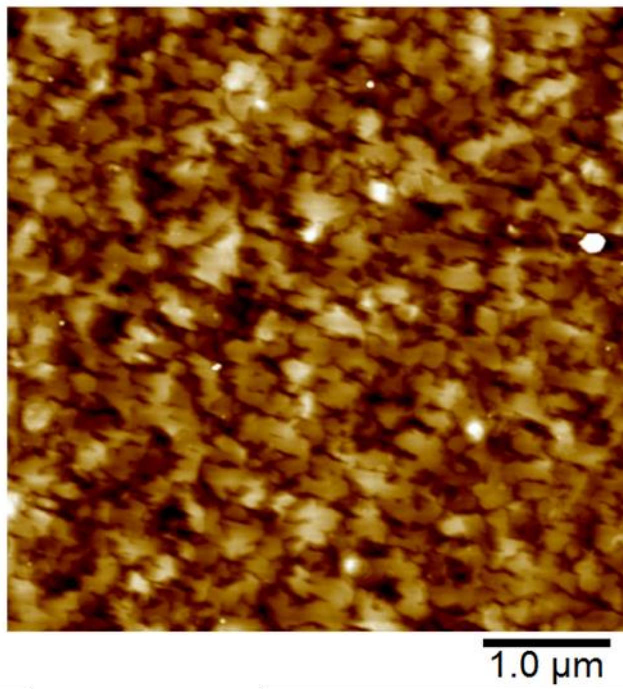

Figure 4-33. 5x5um2 AFM image for AlN:Er (24).

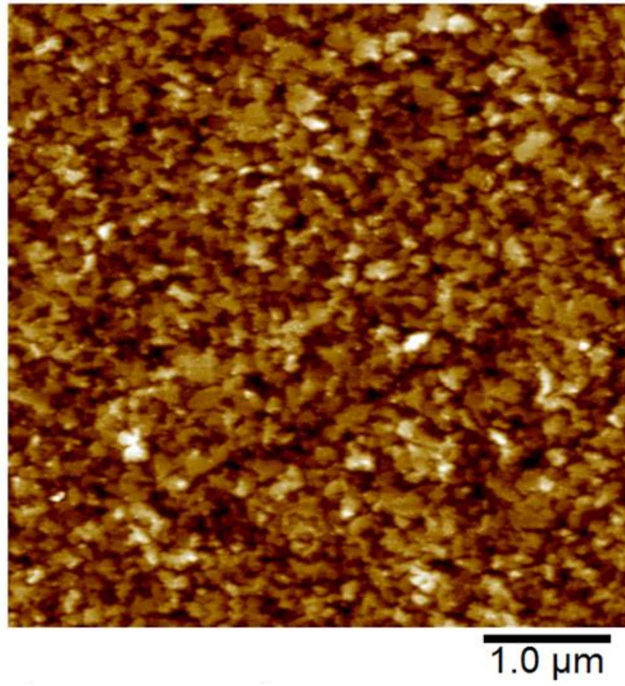

Figure 4-34. 5x5um2 AFM image for AlN:Er (28).

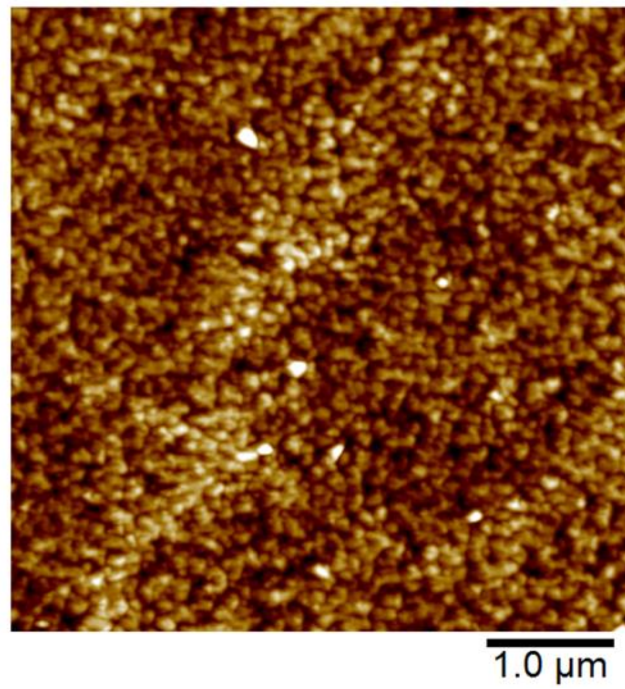

Figure 4-35. 5x5um2 AFM image for AlN:Er (32).

5. Optical properties

Photoluminescence measurements were performed by PL spectrometer MapleII DongWoo Optron using 532nm laser as an excitation source and InGaAs detector operating at -30°C. Part of this thesis was the upgrade of the PL spectrometer to perform measurements in the infrared range by changing the detector, Longwavepass filter and performing the reconfiguration. The wavelength of Er PL characteristic emission is 1.54µm; this emission is related to the electrons transition from energy level $^4I_{13/2}$ to energy level $^4I_{15/2}$. In order to study the impact of the Er flux on the PL intensity all other growth conditions were kept the same. The Photoluminescence scans for all AlN:Er samples were performed from 1.44 to 1.64µm. Figures 4-36 to 4-39 show respectively the PL scans for Er:AlN (20), Er:AlN (24), Er:AlN (28), Er:AlN (32). Upgarding the PL system and performing the scans was part of this thesis.

The PL results of the Er:AlN samples show the unique PL emission feature of the Erbium from 1.5 to 1.6µm. The emission shape is kept the same for all samples which means that the Er flux didn't affect the emission wavelength distribution; however, the Er flux has a clear influence on the intensity. Increasing the Er flux increases the 1.54um emission intensity as shown in figure 4-40.

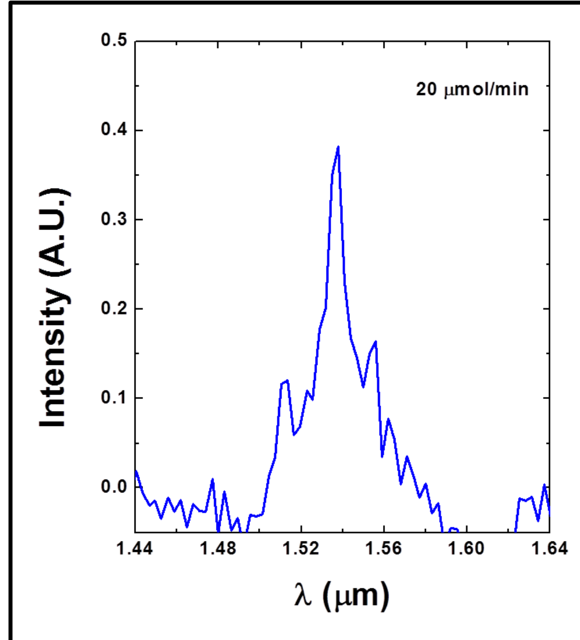

Figure 4-36. PL scan of Er emission at 1540 nm for AlN:Er (20)

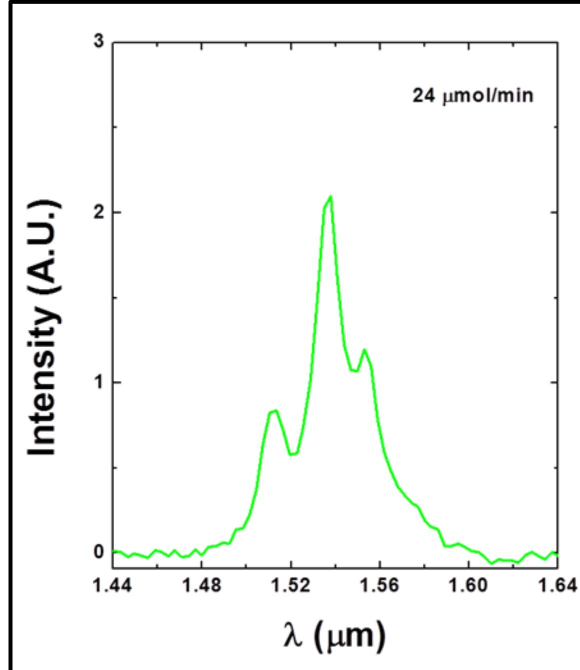

Figure 4-37. PL scan of Er emission at 1540 nm for AlN:Er (24).

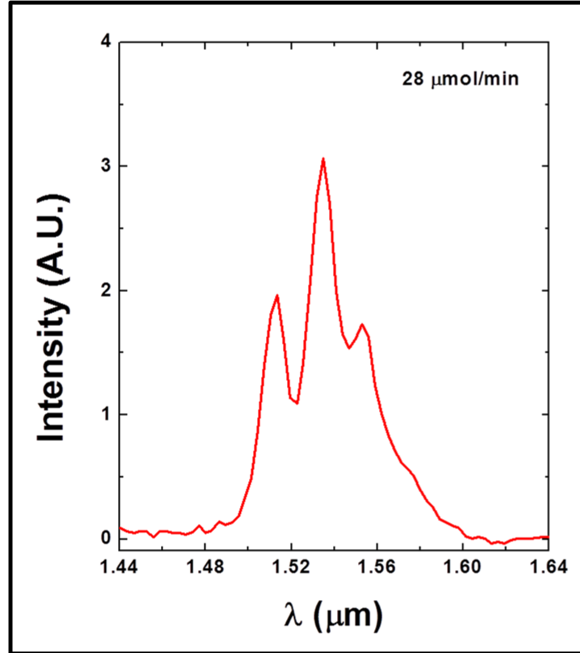

Figure 4-38. PL scan of Er emission at 1540 nm for AlN:Er (28)

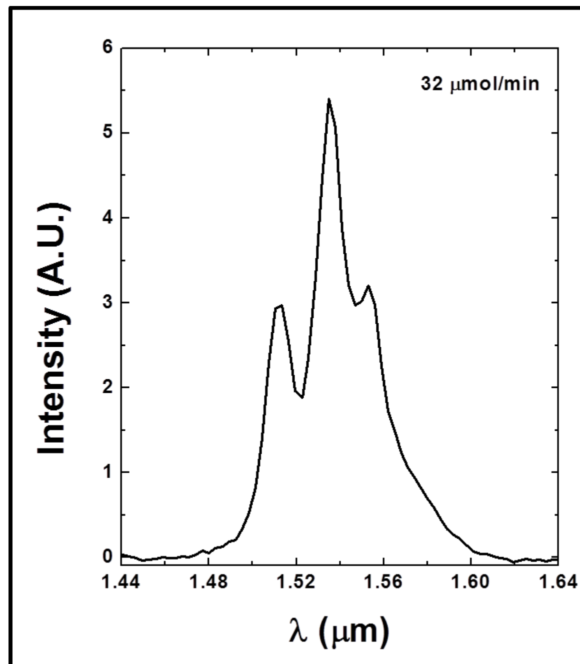

Figure 4-39. PL scan of Er emission at 1540 nm for AlN:Er (32).

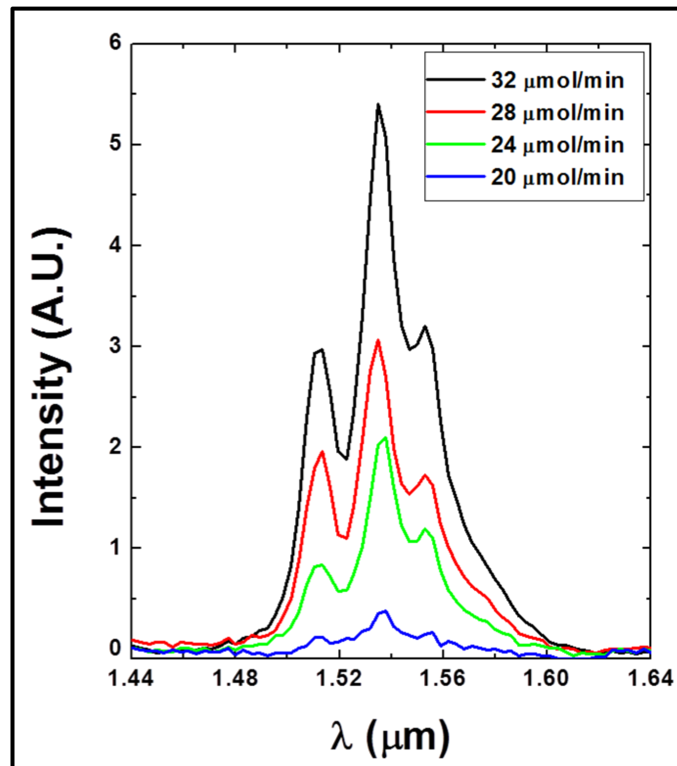

Figure 4-40. PL scan of Er emission overlay at 1540 nm for all AlN:Er samples.

CHAPTER 5: CONCLUSION

MOCVD grown samples with different Er flux were prepared to study the effects of Er flux on the structural and optical properties of AlN:Er. The XRD patterns of Er:AlN samples exhibit high crystalline structure and absence of secondary phases. The rocking curve measurements revealed that the FWHM of Er:AlN samples increases when the Er flux increases and crystalline quality decreases as the Er flux increases. Thus Er doping reduces the crystalline quality of the host AlN thin film. It was observed that the surface morphology changes as a function of Er flux; the island-like feature concentration slightly increases as Er flux increases. Roughness measurements using root mean squared parameter showed that the surface roughness increases when Er flux increases. TOF-SIMS measurements coupled with depth profiling using O_2 sputtering source showed that the Er is uniformly distributed over the doped AlN:Er layer, Al and N profiles exhibit the uniformity of AlN layer throughout the depth. TOF-SIMS signal comparison between AlN:Er (28) and AlN:Er (32) samples showed similar profile shape, however, the TOF-SIMS intensity for AlN:Er (32) is higher for AlN:Er (28) which confirms as expected that the growth conditions are reproducible and that increasing the Er flux during the growth increases the Er concentration in AlN:Er layer. TOF-SIMS measurements coupled with depth profiling confirmed the expected target thickness of AlN:Er which is 300nm by measuring the final depth of the crater using optical profiler and converting the sputtering time to depth. XPS survey scan showed that the present elements on the surface are mainly Al, N, O and C. XPS narrow scans provided surface quantitative measurement for AlN:Er (32) sample. Atomic concentrations for major elements (the ones with atomic

concentration higher than 0.5%) were presented. PL scans exhibited that the shape of Er emission at 1540nm is not affected by Er flux and that Er emission intensity increases with increasing the Er flux.

FUTURE WORK

It is established that increasing Er flux increases Er emission intensity at 1540 nm. Thus, more optimization for AlN:Er growth conditions is required in order to enhance the structural properties for AlN:Er high crystalline quality at high Er flux and to implement these optimized conditions in device application.

REFERENCES

[01] J. M. Zavada, S. X. Jin, N. Nepal, H. X. Jiang, J. Y. Lin, P. Chow, and B. Hertog, "Electroluminescent properties of erbium-doped III–N light-emitting diodes," Appl. Phys. Lett. 84(7), 1061 (2004).

[02] M. R. Brown, A. F. J. Cox, W. A. Shand, and J. M. Williams, "The spectroscopy of rare earth doped chalcogenides," Advances in Quantum Electronics 2, 69–155 (1974).

[03] A. J. Steckl, J. Heikenfeld, M. Garter, R. Birkhahn, and D. S. Lee, "Rare earth doped gallium nitride – light emission from ultraviolet to infrared," Compound Semiconductor 6(1), 48 (2000).

[04] H. Ennen, J. Schneider, G. Pomrenke, and A. Axmann, "1.54-μm luminescence of erbium-implanted III-V semiconductors and silicon," Appl. Phys. Lett. 43(10), 943 (1983).

[05] M. Thaik, U. Hommerich, R. N. Schwartz, R. G. Wilson, and J. M. Zavada, "Photoluminescence spectroscopy of erbium implanted gallium nitride," Appl. Phys. Lett. 71(18), 2641 (1997).

[06] J. T. Torvik, R. J. Feuerstein, J. I. Pankove, C. H. Qiu, and F. Namavar, "Electroluminescence from erbium and oxygen coimplanted GaN," Appl. Phys. Lett. 69(14), 2098 (1996).

[07] C. Ugolini, N. Nepal, J. Y. Lin, H. X. Jiang, and J. M. Zavada, "Excitation dynamics of the 1.54 μm emission in Er doped GaN synthesized by metal organic chemical vapor deposition," Appl. Phys. Lett. 90(5), 051110 (2007).

[08] C. Ugolini, N. Nepal, J. Y. Lin, H. X. Jiang, and J. M. Zavada, "Erbium-doped GaN epilayers synthesized by metal-organic chemical vapor deposition," Appl. Phys. Lett. 89(15), 151903 (2006).

[09] J. M. Zavada and D. Zhang, "Luminescence properties of erbium in III–V compound

semiconductors," Solid-State Electron. 38(7), 1285–1293 (1995).

[10] P. N. Favennec, H. L'Halidon, M. Salvi, D. Moutonnet, and Y. Le Guillou, "Luminescence of erbium implanted in various semiconductors: IV, III-V and II-VI materials," Electron. Lett. 25(11), 718–719 (1989).

[11] Talal Mohammed Al Tahtamouni, Xiaozhang Du, Jingyu Lin and Hongxing Jiang, "Erbium-doped AlN epilayers synthesized by metal-organic chemical vapor deposition" - Vol. 5, No. 3 OPTICAL MATERIALS EXPRESS 648 (2015).

[12] Talal Mohammed Al Tahtamouni, Xiaozhang Du, Jing Li, Jingyu Lin and Hongxing Jiang – "Erbium-doped a-plane GaN epilayers synthesized by metal-organic chemical vapor deposition" Vol. 5, No. 2 OPTICAL MATERIALS EXPRESS 274 (2015).

[13] Neelam Kumari, Ashwini K. Singh and P.K. Barhai, - "Study of Properties of AlN Thin Films Deposited by Reactive Magnetron Sputtering" Int. J. Thin Fil. Sci. Tec. 3, No. , 43-49 (2014).

[14] R. D. Vispute, Hong Wu, and J. Narayan, - "High quality epitaxial aluminum nitride layers on sapphire by pulsed laser deposition" J. Appl. Phys., Vol.77, No. 9 (1995).

[15] R. G. Wilson, R. N. Schwartz, C. R. Abernathy, S. J. Pearton, N. Newman, M. Rubin, T. Fu, and J. M. Zavada, "1.54-μm photoluminescence from Er-implanted GaN and AlN," Appl. Phys. Lett. 65(8), 992 (1994).

[16] F. S. Liu, Q. L. Liu, J. K. Liang, J. Luo, H. R. Zhang, Y. Zhang, B. J. Sun, and G. H. Rao, "Visible and infrared emissions from c-axis oriented AlN:Er films grown by magnetron sputtering," J. Appl. Phys. 99(5), 053515 (2006).

[17] J. H. Edgard (Ed.), Properties of Group-III Nitrides, EMIS Data reviews Series, IEE, London (1994).

[18] T. P. Chow, R. Tyagi, "Wide bandgap compound semiconductors for superior high-voltage power devices", IEEE Trans. Electron Devices, vol. 41, pp. 1481-1482, 1994.

[19] M. A. Khan, Q. Chen, J. W. Yang, M. S. Shur, B. T. Dermott and J. A. Higgins, "Microwave Operation of GaN/AlGaN Doped Channel Heterostructure Field Effect Transistors," IEEE Electron Device Letters, vol. 17, No. 7, pp. 325-327, July (1996).

[20] S. Nakamura and G. FasOl, "The Blue Laser Diode" (Springer, New York, 1997).

[21] L. F. Eastman and U. K. Mishra, "The toughest transistor yet [GaN transistors]" IEEE Spectr. 39, 28 (2002).

[22] W. C. Johnson, J. Parsons, and M. C. Crew, "Nitrogen Compounds of Gallium" J. Phys. Chem. 36, 2561 (1932).

[23] R. Juza and H. Hahn, Z. Anorg. Allgem. Chem. 234, 282 (1938).

[24] H. P. Maruska and J. J. Tietjen, "The Preparation and Properties of Vapor-Deposited Single-Crystal GaN" Appl. Phys. Lett. 15, 327 (1969).

[25] M. Ilegems and R. Dingle, "Luminescence of Be- and Mg-doped GaN" J. Appl. Phys. 44, 4234 (1973).

[26] J. I. Pankove, M. T. Duffy, E. A. Miller, and Berkeyhelser, J. Lumin. 8, 89 (1973).

[27] O. Lagerstedt and B. Monemar, "Luminescence in epitaxial GaN : Cd" J. Appl. Phys. 45, 2266 (1974).

[28] B. Monemar, O. Lagerstedt, and H. P. Gislason, "Properties of Zn-doped VPE-grown GaN. I. Luminescence data in relation to doping conditions" J. Appl. Phys. 51, 625 (1980).

[29] J. I. Pankove and J. A. Hutchby, "Photoluminescence of ion-implanted GaN" J. Appl. Phys. 47, 5387 (1976).

[30] H. Amano, I. Akasaki, K. Hiramatsu, and N. Koide, Thin Solid Films 163, 415 (1988).

[31] I. Akasaki, H. Amano, Y. Koide, K. Hiramatsu, and N. Sawaki, "Effects of AlN buffer layer on crystallographic structure and on electrical and optical properties of GaN and Ga1-

xAlxN (0<x≦0.4) films grown on sapphire substrate by MOVPE” J. Cryst. Growth 98, 209 (1989).

[32] S. Nakamura, “GaN Growth Using GaN Buffer Layer” Jpn. J. Appl. Phys., Part 2 30, L1705 (1991).

[33] S. Nakamura, M. Senoh, and T. Mukai, “Highly P-Typed Mg-Doped GaN Films Grown with GaN Buffer Layers” Jpn. J. Appl. Phys., Part 2 30, L1708 (1991).

[34] Pearson’s Crystal Data.

[35] H. Morkoc, Nitride Semiconductor and Devices, Springer, Berlin Germany, (1999).

[36] D. Zhuang, j.h. Edgar “Wet etching of GaN, AlN, and SiC: a review” - materials science and engineering: R: reports, vol. 48, issue 1, pages 1 – 46 (2005).

[37] B. Monemar, “Luminescence in III-nitrides”, materials science and Engineering B59, 122 (1999).

[38] A. H. Kitai (Ed), “Solid State Luminescence; Theory, Materials and Devices”, Springer, New York, (1993).

[39] M. Maqbool, “Growth, Characterization and Luminescence and optical properties of Rare earth elements and transition metals doped in wide Band gap Nitride semiconductor”, Dissertation (2009).

[40] G.A. Slack and-T.F. McNelly, “Aluminium Nitride Crystal Growth” J. Crystal Growth, 42, 5 60 (1977).

[41] G. C Yi (Ed), “Semiconductor Nanostructures for Optoelectronic Devices: Processing, Characterization and Application; Nanoscience and Technology”, Springer, New York, (2012).

[42] R. D Vispute “Epitaxial growth of AlN thin films on Silicon (111) substrates by Pulsed Laser deposition”, J. Appl. Phys., Vol.77, No. 9 (1995).

[43] http://www.ioffe.ru

[44] http://www.pveducation.com

[45] A. R. Zanatta and L. A. Nunes, “Green photoluminescence from Er-containing amorphous SiN thin films” Appl. Phys. Lett. 72, 3127 (1998).

[46] A. J. Steckl and R. Birkhahn “Visible emission from Er-doped GaN grown by solid source molecular beam epitaxy” Appl. Phys. Lett. 73, 1700 (1998).

[47] G. B. Stringfellow “Technologies Based on Organometallic Vapor Phase Epitaxy” Volume 210 of the series NATO ASI Series pp 303-316 ISBN978-1-4612-7861-0 (1989).

[48] Veeco instruments Inc.

[49] T. Metzger, R. Höpler, E. Born, O. Ambacher, M. Stutzmann, R. Stömmer, M. Schuster, H. Göbel, S. Christiansen, M. Albrecht and H. P. Strunk, “Defect structure of epitaxial GaN films determined by transmission electron microscopy and triple-axis X-ray diffractometry” Philos. Mag. A **77**, No 4, 1013 (1998).

[50] Bruker Corporation.

[51] Dongwoo Optron Co.

[52] Evans Analytical Group.

[53] Thermo Fisher Scientific.

[54] http://www.geobiologie.uni-goettingen.de

[55] IonTOF GmbH.

[56] http://www.nanoscience.co.jp

[57] FEI (part of Thermo Fisher Scientific).

[58] Manuel Garcia-Mendez “Controlled Growth of C-Oriented AlN Thin Films: Experimental Deposition and Characterization” ISBN: 978-953-307-610-2, InTech (2012).

[59] I. STANCA, “CHEMICAL STRUCTURE OF AlN FILMS GROWN BY LASER ABLATION: AN X-RAY PHOTOELECTRON SPECTROSCOPY STUDY”, Rom. Journ. Phys., Vol. 49, Nos. 9–10, P. 807–815, Bucharest, (2004).

[60] Tamotsu Hashizume, Shinya Ootomo, Takanori Inagaki and Hideki Hasegawa, “Surface

passivation of GaN and GaN/AlGaN heterostructures by dielectric films and its application to insulated-gate heterostructure transistors", J. Vac. Sci. Technol. B 21(4) - Jul/Aug 2003.